Solid Earth

Open Access

EGU

High stresses stored in fault zones: example of the Nojima fault (Japan)

Anne-Marie Boullier[1]**, Odile Robach**[2]**, Benoît Ildefonse**[3]**, Fabrice Barou**[3]**, David Mainprice**[3]**, Tomoyuki Ohtani**[4]**, and Koichiro Fujimoto**[5]

[1]ISTerre, Univ. Grenoble Alpes, CNRS, 38000 Grenoble, France
[2]CEA, INAC-MEM, Univ. Grenoble Alpes, 38000 Grenoble, France
[3]Géosciences Montpellier, CNRS, Univ. Montpellier, 34095 Montpellier, France
[4]Department of Civil Engineering, Gifu University, Gifu 501-1193, Japan
[5]Faculty of Education, Tokyo Gakugei University, Tokyo, Japan

Correspondence: Anne-Marie Boullier (anne-marie.boullier@univ-grenoble-alpes.fr)

Abstract. During the last decade pulverized rocks have been described on outcrops along large active faults and attributed to damage related to a propagating seismic rupture front. Questions remain concerning the maximal lateral distance from the fault plane and maximal depth for dynamic damage to be imprinted in rocks. In order to document these questions, a representative core sample of granodiorite located 51.3 m from the Nojima fault (Japan) that was drilled after the Hyogo-ken Nanbu (Kobe) earthquake is studied by using electron backscattered diffraction (EBSD) and high-resolution X-ray Laue microdiffraction. Although located outside of the Nojima damage fault zone and macroscopically undeformed, the sample shows pervasive microfractures and local fragmentation. These features are attributed to the first stage of seismic activity along the Nojima fault characterized by laumontite as the main sealing mineral. EBSD mapping was used in order to characterize the crystallographic orientation and deformation microstructures in the sample, and X-ray microdiffraction was used to measure elastic strain and residual stresses on each point of the mapped quartz grain. Both methods give consistent results on the crystallographic orientation and show small and short wavelength misorientations associated with laumontite-sealed microfractures and alignments of tiny fluid inclusions. Deformation microstructures in quartz are symptomatic of the semi-brittle faulting regime, in which low-temperature brittle plastic deformation and stress-driven dissolution-deposition processes occur conjointly. This de-

formation occurred at a 3.7–11.1 km depth interval as indicated by the laumontite stability domain.

Residual stresses are calculated from deviatoric elastic strain tensor measured using X-ray Laue microdiffraction using the Hooke's law. The modal value of the von Mises stress distribution is at 100 MPa and the mean at 141 MPa. Such stress values are comparable to the peak strength of a deformed granodiorite from the damage zone of the Nojima fault. This indicates that, although apparently and macroscopically undeformed, the sample is actually damaged. The homogeneously distributed microfracturing of quartz is the microscopically visible imprint of this damage and suggests that high stresses were stored in the whole sample and not only concentrated on some crystal defects. It is proposed that the high residual stresses are the sum of the stress fields associated with individual dislocations and dislocation microstructures. These stresses are interpreted to be originated from the dynamic damage related to the propagation of rupture fronts or seismic waves at a depth where confining pressure prevented pulverization. Actually, M6 to M7 earthquakes occurred during the Paleocene on the Nojima fault and are good candidates for inducing this dynamic damage. The high residual stresses and the deformation microstructures would have contributed to the widening of the damaged fault zone with additional large earthquakes occurring on the Nojima fault.

1 Introduction

Using near-field seismic data recorded during earthquakes, it is possible to derive kinematic rupture models describing the spatial distribution of slip, rupture time, and rise time on the fault. Inversion of such models allows the determination of the space–time history of shear stress on the fault plane during the rupture. As an example, dynamic shear stress drop calculated for four well-instrumented large earthquakes on the San Andreas Fault system varies from 20 to 100 MPa (Bouchon, 1997). These values are very heterogeneous along the fault plane and can be regarded as a lower bound because of the limited spatial resolution of the kinematic models, which is at best a few kilometers. If the shear stress drop can be evaluated, the ordinary stress levels in the crust need to be measured in situ in deep wells and boreholes using a hydraulic fracturing technique and analysis of stress-induced well bore breakouts (Zoback and Healy, 1992) or by anelastic strain recovery measurements on cores retrieved from boreholes (Lin et al., 2006). Behavior of a rock submitted to a tectonic (quasi-static) or seismic (dynamic) loading will depend on the loading history and residual stresses stored in the rock, which may be defined as the stresses remaining in the rock when all the applied stresses have been removed. Chen et al. (2015) measured up to 300 MPa residual stress in quartz fragments within the damage zone of the San Andreas Fault at 2.7 km of depth (ca. 100 MPa confining pressure) using X-ray Laue microdiffraction. This residual stress value is higher than the ≈ 60 MPa differential stress deduced from in situ measurements at 1671 m of depth in the nearby SAFOD pilot hole (Hickman and Zoback, 2004).

Considering this high level of residual stress, large damage is expected in rocks surrounding a fault. Actually, when an earthquake occurs, displacement is localized on a very thin (< 10 mm) slip zone (Chester and Chester, 1998; Sibson, 2003) in which a gouge is formed by friction-related grain size reduction (Sibson, 1977). Outside the fault core, 1 to 10^3 m wide zones may be damaged by brittle failure of the surrounding rocks. Recently, several examples of pulverized rocks lacking significant shear have been described at the surface or subsurface within 100 to 200 m wide bands close to large faults such as the San Andreas Fault (Dor et al., 2006; Rockwell et al., 2009; Wechsler et al., 2011) or the Arima–Takatsuki Line in Japan (Mitchell et al., 2011) and have been attributed to dynamic coseismic damage. At the same time, high-strain-rate experiments on granite using Hopkinson bars without confinement have reproduced similar pulverized rocks (Xia et al., 2008) and predicted a dynamic strain rate threshold for pulverization (Doan and Gary, 2009). Below the pulverization threshold, fractures without shear are formed in the samples, which remain cohesive. Yuan et al. (2011) have performed similar experiments under confinement and did not observe pulverization under 132 MPa, which was the maximum confining pressure allowed by their apparatus. They suggest, therefore, that with increasing confining pressures, the strain rate threshold increases as well and that coseismic pulverization process is restricted to the uppermost crust (≤ 3 km or ~ 100 MPa confining pressure; see review in Aben et al., 2017). Until now, pulverized rocks have been mostly observed at shallow levels, although a few cases of coseismic off-fault damage at depth are documented in the literature. Fragmentation of garnet at very high stresses and strain rates at depth corresponding to temperatures of about 300–350 °C was first described by Trepmann and Stöckert (2002) in the Sesia Zone (Italian Alps). More recently, Sullivan and Peterman (2017) documented an example of granite pulverized at the brittle–ductile transition (400 °C, 200 MPa) in the 50–200 m wide damage zone of the Kellyland fault (eastern Maine, USA). Garnet fragmentation associated with pseudotachylites in the western Norway eclogitic crust was attributed to deep crustal earthquakes (Austrheim et al., 2017). Concerning carbonate lithologies, Sagy and Korngreen (2012) described dynamically fractured rocks in a deep borehole at 5 km depth in Israel.

In this paper, we will investigate the natural deformation microstructures of a representative sample located in the hanging wall of the Nojima fault zone (Japan). The studied sample was slightly deformed at depth, then exhumed by uplift and erosion, and collected by the Geological Survey of Japan (GSJ) in the Hirabayashi drill hole. We will compare the deformation microstructures of that sample with experimentally produced microstructures during dynamic loading and with naturally fragmented fault rocks described in the literature.

Techniques of petrographic microscopy, scanning electron microscopy (SEM) and cathodoluminescence were used to characterize microstructures, microfractures and their cement. Electron backscattered diffraction (EBSD) and X-ray Laue microdiffraction were used to characterize the intragranular heterogeneities of crystallographic orientation in quartz grains and to map the elastic strains and residual stresses. The complexity of the later technique is the reason for studying a unique but representative sample in detail. We will compare our results with those obtained by Chen et al. (2015) on a sample of the San Andreas Fault zone. Then we will discuss the significance of these results in terms of stress and strain rate (quasi-static or dynamic) and the contribution of the observed microscopic damage to the widening of the damaged fault zone.

2 Geological setting

The Nojima Fault is a 45° N-striking and 85° SE-dipping dextral reverse fault (Fig. 1) on which the 1995 Hyogo-ken Nanbu earthquake occurred (Kobe earthquake, M7.2). The fault cuts across the Cretaceous Ryoke granodiorite. The GSJ successfully drilled the Hirabayashi borehole through the Nojima Fault on Awaji Island 1 year after the earth-
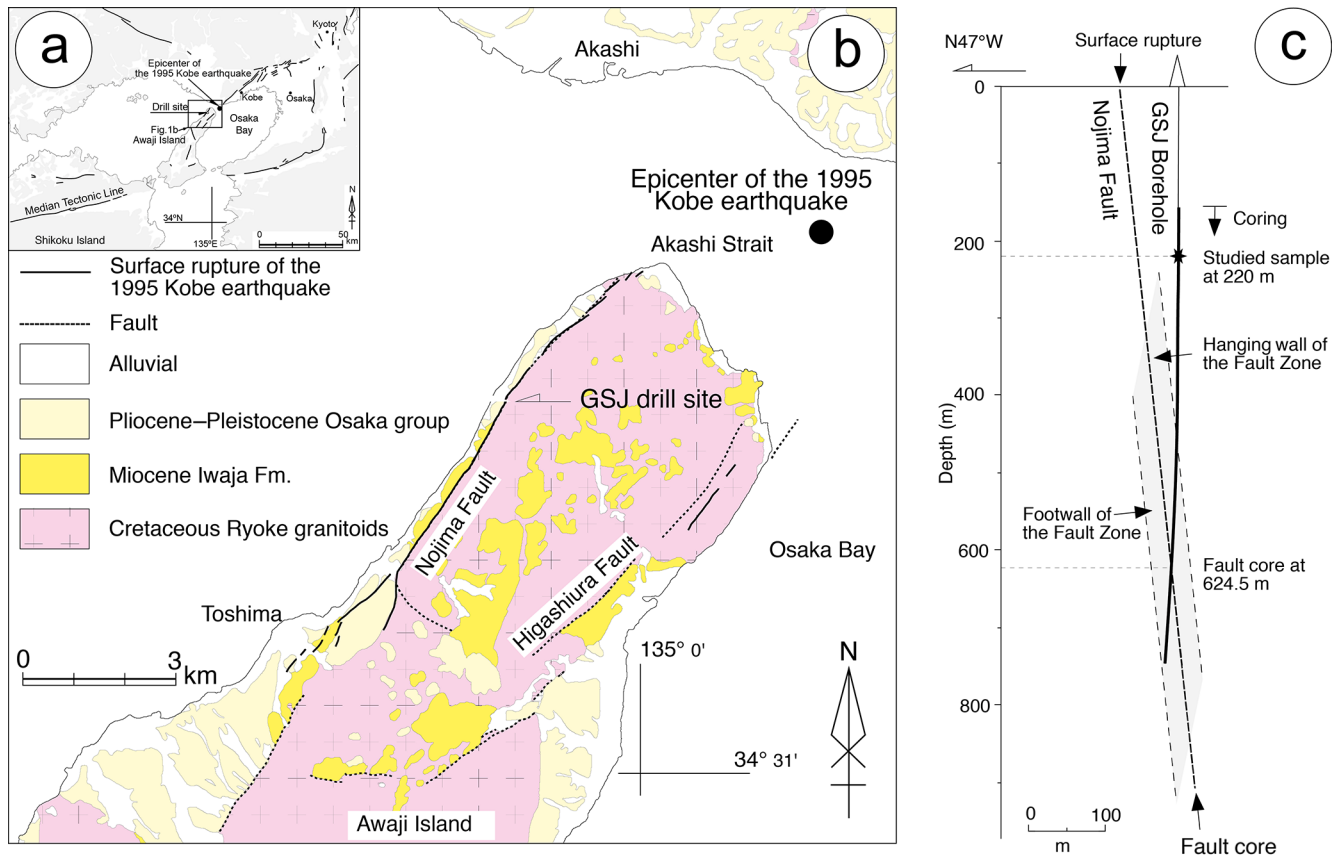
Figure 1. Geological setting (modified from Ohtani et al., 2000a). **(a)** Insert showing the localization of Awaji Island. **(b)** Geological map of Awaji Island showing the Nojima fault and the location of the GSJ Hirabayashi drill hole. **(c)** Schematic cross section showing the relative geometries of the Nojima fault and the GSJ drill hole.

quake. Cores were recovered for almost the entire depth interval from 150 to 746.6 m due to the cohesion of the rocks (Ito et al., 2000). The drill hole sampled the principal slip zone (PSZ) of the Kobe earthquake at 624.5 m depth (Fig. 1c; Ohtani et al., 2000a; Tanaka et al., 2001). Two major periods of seismic activity on the fault separated by an exhumation of the basement of Awaji Island were inferred using the relationships between hydrothermal minerals and deformation microstructures (Boullier et al., 2004a; Boullier, 2011). The first period of seismic activity was characterized by pseudotachylites and by laumontite as the main sealing mineral of the fractures. Laumontite is a zeolite ($Ca_4(Al_8Si_{16}O_{48}) \cdot 18H_2O$) which crystallizes from aqueous fluids in the 100–300 MPa pressure range and at temperatures lower than 300 °C (Cho et al., 1987). This fixes the depth range of laumontite precipitation and laumontite-associated deformation to a 3.7 to 11.1 km depth interval using a rock density of 2.7 g cm^{-3} and a lithostatic pressure gradient. This first period of seismic activity has been dated around 56 Ma by fission tracks in zircon (Murakami and Tagami, 2004). The second period (≤ 1.2 Ma) was characterized by carbonates precipitating in coseismic fractures

(Boullier et al., 2004b) and whose composition is consistent with the fluids circulating within the fault today (Fujimoto et al., 2007). This two-stage tectonic history of the Nojima fault is compatible with the regional structural analysis (Kanaori, 1990; Fabbri et al., 2004; Famin et al., 2014), which reveals a sinistral wrenching in the Paleogene (65 to 23 Ma), followed by fault-normal extension in the Miocene (23 to 6 Ma) and a dextral slip active since the Plio-Quaternary (≤ 2 Ma).

In the present paper, we focus on deformation microstructures formed during the first period of seismic activity. The studied sample was in the 3.7–11.1 km depth range, as constrained by the laumontite stability field, before being exhumed and sampled at 220 m of depth by the GSJ drill hole (Fig. 1c). By comparing conductive planes detected by the Fullbore Formation MicroImager (FMI, trademark of Schlumberger) with open fractures on 360° azimuthal core scanner images, it was possible to reorient most sections of the drill core (Ohtani et al., 2000b). Therefore, microstructures observed in the studied sample could be geographically oriented, which is not usually the case.

3 Analytical procedures

3.1 EBSD

Small-scale observations were performed on polished thin sections (100 μm thick) cut perpendicular to the drill-core axis, i.e., close to the horizontal plane. Examination with a petrographic microscope was used to recognize the characteristic microstructural features and sealing minerals.

Crystallographic orientation of quartz was determined using indexation of EBSD patterns using the Camscan CrystalProbe X500FE SEM (Géosciences Montpellier, CNRS, Université de Montpellier), equipped with an EBSD HKL NordlysNano detector for crystallographic analysis and an energy dispersive spectroscopy X-Max^N 20 mm^2 detector for chemical analysis, with both driven by the Aztec software (Oxford Instruments). Diffraction patterns were generated at 20° tilted incident electron beam with a carefully polished horizontal thin section (note this equivalent to 70° tilt of conventional SEM). The orientation maps were obtained in automatic acquisition mode with a step size of 4 or 0.5 μm for detailed areas. Standard post-acquisition data processing was performed using the Tango software of the Channel 5® suite (HKL Technology) to (i) remove isolated pixels that are indexed as a given phase and surrounded by either non-indexed pixels or pixels indexed for another phase or (ii) fill non-indexed pixels that have a minimum of 6 neighboring pixels with the same orientation, EBSD data processing was then performed using the MTEX open-source MATLAB toolbox (version 4.3.1; http://mtex-toolbox.github.io/, last access: 11 April 2018; Hielscher and Schaeben, 2008; Bachmann et al., 2010; Mainprice et al., 2014).

3.2 Laue X-ray microdiffraction

Laue X-ray microdiffraction maps were collected on the same thin section as for EBSD using the synchrotron X-rays of a bending magnet at the ESRF (Grenoble) and the apparatus of the CEA-CNRS CRG-IF BM32 beamline following a method described by Ulrich et al. (2011) and Robach et al. (2017). The 0.5×0.5 μm^2 polychromatic (5 to 22 keV) horizontal X-ray beam impinges the sample surface inclined at a 40° angle (Fig. 2a). The Laue patterns were collected on a MAR 165 CCD camera with 165 mm diameter and 2048×2048 pixels at 70 mm to the sample (Fig. 2b), mounted around a diffraction angle of 2θ of 90° (in reflection geometry). The geometry of the diffraction experiment was calibrated using the Laue pattern of a single Ge crystal, as described in Ulrich et al. (2011). The sample was scanned in front of the X-ray microbeam for mapping using a high-resolution x–y stage. Exposure time at each x-y point was 0.2 s. The probing depth in the investigated X-ray transparent material (quartz) was limited by the thickness (100 μm) of the thin section. Depending on the (x, y) position of the
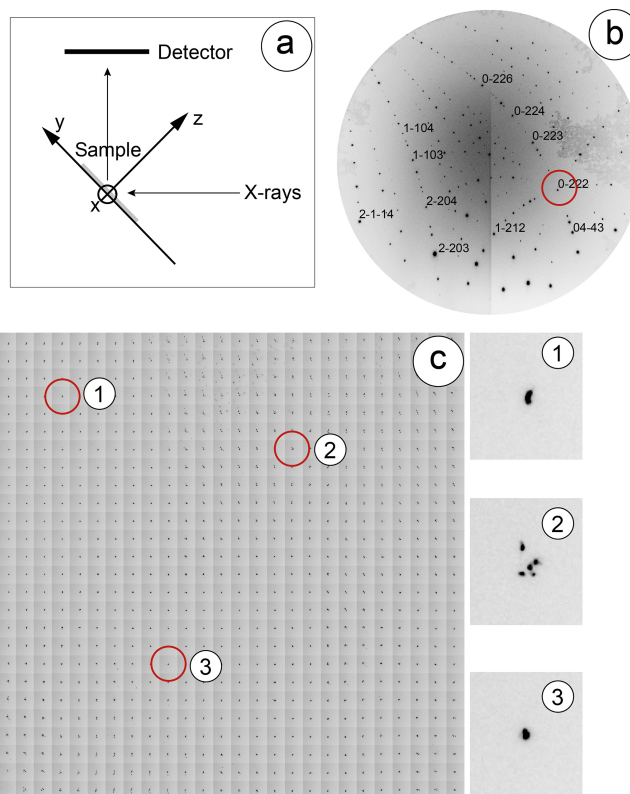
Figure 2. X-ray Laue microdiffraction. **(a)** Geometric disposition of the sample relative to the X-ray's beam and definition of the x, y and z axes of the sample referential. A more detailed definition of the sample reference frame is provided in Petit et al. (2015). **(b)** Laue image corresponding to the point indicated by the red circle 3 on the map; some spots are indexed, especially the (0-222) spot (red circle), which has been used for the following mosaic map. The detector image is oriented as the one that would be seen by an observer lying at the place of the sample and receiving the incident beam on the top of the head. Panel **(c)** shows a 26×26 point mosaic map constructed with a 10 μm step on the quartz grain analyzed in Fig. 4. The (0-222) spot location, shape and intensity of the detector vary for each step depending on the orientation, crystallinity and deformation of the crystal. In point 2 of the map, multiple spots are indicative of several subgrains present in the analyzed volume; in point 1, the (0-222) spot is elongated in a NNW–SSE direction indicating a continuous bending of the crystal lattice roughly around the x axis (Robach et al., 2017).

probe, quartz deformation, single spots (one crystallite) or multiple spots (several subgrains) were obtained (Fig. 2c).

Automated analysis of Laue patterns comprises different stages that were described in Tamura (2014) for XMAS software and Robach et al. (2017) for LaueTools software (http://sourceforge.net/projects/lauetools/, last access: 19 April 2018). Here LaueTools software was used for the Laue pattern indexation, determination of the crystal Euler angles (orientation) and the distortion of the quartz unit cell (deviatoric elastic strain, obtained by comparing the experimental

and the undeformed unit cell). The details of the data analysis are explained in the Appendix A1. As pointed out by Chen et al. (2012), when indexing the Laue spots, it is impossible to lift the ambiguity between a crystal and its Dauphiné twin (rotated by 180° around c axis) by using only the spot positions, and spot intensities need to be exploited (see Appendix A2 for details).

4 Characterization of microstructures

The NOJ220 sample studied in this paper is a macroscopically undeformed granodiorite located outside the damage fault zone at 220 m depth in the borehole and a distance of $d_{\text{fault}} = 51.3$ m to the fault plane in the hanging wall (see Fig. 1c). It shows a typical isotropic magmatic structure and contains the following minerals: orthose, plagioclase, hornblende, biotite, centimeter-sized quartz and accessory minerals such as zircon, apatite, titanite and allanite. Plagioclase, hornblende and biotite appear as gray, green and brown, respectively, on the thin section (Fig. 3a). Deformation microstructures are omnipresent when observed under the microscope. They are described below.

4.1 Laumontite-filled veins

Two types of laumontite-filled veins are defined depending on their size. The first type is represented by wide (up to 1 mm) and long (more than 3 cm, the thin section length) veins, which are indicated by yellow arrows in Fig. 3a. They are generally straight or slightly curved, E–W striking and 70° southward dipping in the geographic frame. They contain large angular fragments of the granodiorite minerals embedded in small (< 0.2 mm) laumontite crystals (Fig. 3b and c). Fragments generally do not touch each other. Biotite fragments are delaminated, as are some biotite crystals immediately adjacent to the veins. The different nature and crystallographic orientation of the fragments compared to the fracture-wall minerals suggest that these fragments have been at least rotated and probably transported some distance from their initial position. The widest veins are clearly dilatant with some shearing component as shown by the deformed cleavages of neighboring biotite crystals. However, the exact opening kinematics cannot be clearly established on the basis of the horizontal thin section alone. These veins may be qualified as breccia-like veins and are similar to those described by Blenkinsop and Sibson (1992, their Fig. 4d) in the core samples from the Cajon Pass drill hole near to the San Andreas Fault.

The second type is represented by veins that are 20–200 μm wide and several centimeters long veins. They are transgranular, straight, or with a jigsaw geometry and are roughly E–W orientated and filled by laumontite prisms. They do not contain fragments and have parallel vein walls (thick black arrows in Fig. 4b; Si, Ca and Al maps in Fig. 4e).
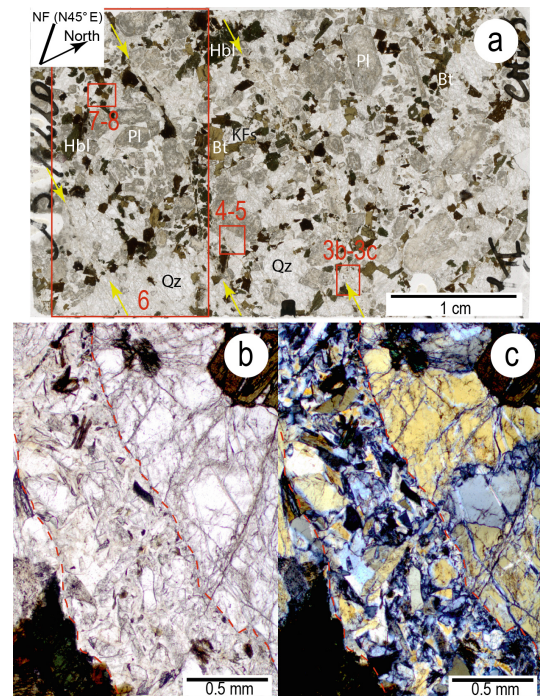

Figure 3. The NOJ220 thin section (45 × 30 mm). **(a)** Scan showing the overall preserved magmatic texture. The orientation of the thin section is inverse and indicated in the top left box (NF: Nojima fault). Brown to black minerals are biotites (Bt) or hornblendes (Hbl). Large grayish minerals are K feldspars (Kfs) or plagioclases (Pl). Light gray minerals are microfractured quartz (Qz). Red rectangles localize Figs. 3b, c, 4a, 6, 7 and 8. Yellow arrows indicate breccia-like laumontite-filled veins. **(b, c)** Microphotographs in plane polarized light **(b)** and crossed polarized light **(c)** of a breccia-like laumontite-filled vein showing the angulous mineral fragments within a laumontite matrix. The red dotted lines locate the vein walls.

In these veins, the prisms of laumontite are generally orientated at a high angle to the vein walls.

4.2 Deformation microstructures in quartz

When observed under the petrographic microscope, quartz grains display a intracrystalline deformation characterized by undulous extinction without dynamic recrystallization. They are also pervasively affected by numerous intragranular microfractures (Fig. 4a) whose 50° N orientation is independent from crystallographic orientation of the host quartz. They are only visible at a small scale (small black arrows in the grain investigated using EBSD, Fig. 4b) and are sealed by laumontite as shown on the Si, Ca and Al maps in Fig. 4c. Nevertheless, quartz grains have preserved their magmatic shape (Fig. 3a), thus indicating a low finite strain.

Fluid inclusions in quartz grains of the NOJ220 sample are unusual. Contrary to fluid inclusions in undeformed quartz-bearing rocks which have generally rounded or negative crys-
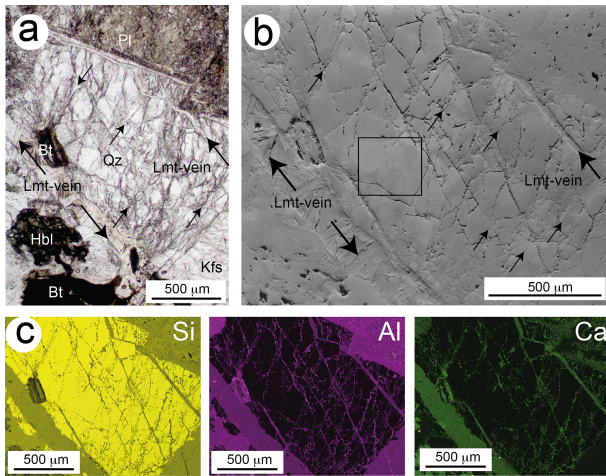
Figure 4. Representative quartz grain (Qz) studied with EBSD (area shown in Fig. 3a). **(a)** Microphotograph (plane polarized light) of the quartz grain bound by laumontite (Lmt) veins (large black arrows) and surrounded by K feldspar (Kfs), plagioclase (Pl), biotite (Bt) and hornblende (Hbl). The quartz grain shows abundant well-oriented intragranular microfractures (small black arrows). **(b)** Forward-scattered electron image of the same area. Thick arrows: intergranular laumontite-filled veins. Thin arrows: intragranular microfractures and alignments of tiny fluid inclusions. The slightly different gray levels are due to different crystallographic orientations. The rectangle locates the subregion finely mapped with EBSD (Fig. 10) and X-ray Laue microdiffraction (Fig. 11). **(c)** Compositional maps of the same area for Si, Ca and Al showing the laumontite-filled veins.

tal shapes (Roedder, 1984), fluid inclusions define short (tens of micrometers) alignments of tiny neonate fluid inclusions (see Fig. S1 in the Supplement). These alignments share the same 50° N orientation parallel to the Nojima fault in all quartz grains independent of the crystallographic orientation of the host quartz (Fig. S1a). They form a continuum with the pervasive intragranular 50° N-oriented healed microfractures, which share the same dark blue signature on the SEM–cathodoluminescence image and are themselves branched on laumontite-filled veins (see Figs. S2 and S3). Our observations indicate that the alignments of tiny fluid inclusions are present in most of the core samples within the 200 to 750 m depth range in the GSJ drill hole.

4.3　Kink bands in biotites

Kinking of (001) cleavage in biotite is a common feature in the NOJ220 sample and in most of the samples along the drill hole (Tanaka et al., 2001). Kink bands are at a high angle to (001) cleavage. They are comparable to kink bands in biotite described in granitic samples from the shock region around a nuclear explosion (Cummings, 1965; Fauré, 1970) or in granite deformed under quasi-static conditions (Amitrano and Schmittbuhl, 2002). They provide a marker to extract the shortening intensity by measurement of the change

in length of (001) cleavages and the direction of compression by measuring the orientation of kink bands (Fig. S1b). Strain recorded by biotite in the NOJ220 sample reaches up to 5 %. Kink bands are roughly 50° N oriented parallel to the alignments of tiny fluid inclusions described above (Fig. S1a) and to the Nojima fault.

5　EBSD measurements in quartz

The first quartz grain investigated using EBSD (Fig. 4) is representative of the average density of microfractures in the NOJ220 sample. The misorientation map (i.e., misorientation of each pixel relative to the mean orientation of the grain, Fig. 5b) shows a chessboard pattern defined by large (50–100 μm) subgrains limited by sharp boundaries which are mostly independent of the microfracture geometry. Smaller misorientation domains are superimposed on this chessboard pattern and are roughly elongated parallel to the microfractures (lower right area in Fig. 5b), but are cross-cut by the microfractures in many places. Misorientation axes for subgrain (either large or small) boundaries showing 0.5 to 5° misorientation are close to the [0001] axis (Fig. 5d). Dauphiné twinning characterized by a rotation of 60° around (0001) is shown on the map of inverse pole figures of the x axis (Fig. 5a) by the small dark green domains. The pole figures (Fig. 5c) are characterized by the superposition of (10-11) and (01-11) in twinned and un-twinned domains when (11-20) and (10-10) remain the same (e.g., Mainprice et al., 1993). Note that the Dauphiné twinned domains are also slightly elongated in the 50° N direction similar to the intragranular microfractures.

Microfractures may be locally very dense as in the 50 to 90° N-oriented array joining one biotite or hornblende to another across the whole thin section (Fig. 6). Figure 7 shows a group of quartz grains along this array, which is squeezed in between a biotite and an amphibole and cut by numerous microfractures radiating in a Hertzian pattern and sealed by laumontite (Ca, Al and Si maps in Fig. 7c). Up to 30 % dilatancy was measured on the SEM image (Fig. 7b) by cumulating the thicknesses of laumontite-filled microfractures on a transect perpendicular to them. This dilatancy may be compared to the average value of 10 % extension measured in several quartz grains. Alignments of tiny fluid inclusions in the neighboring quartz have a strong 50° N orientation and display the same dark-blue cathodoluminescence signature as the healed microfractures, which are themselves in continuity with the laumontite-sealed microfractures (see Fig. S3). Only the quartz grains were selected for the EBSD map. EBSD measurements of the three quartz grains reveal Dauphiné-twinned domains (Fig. 8a) showing the same crystallographic relationships as in the previous example (see pole figures in Fig. 8c) and misorientation domains (Fig. 8b). As for the quartz grain investigated in Fig. 5, large subgrains define a chessboard pattern independent of the mi-
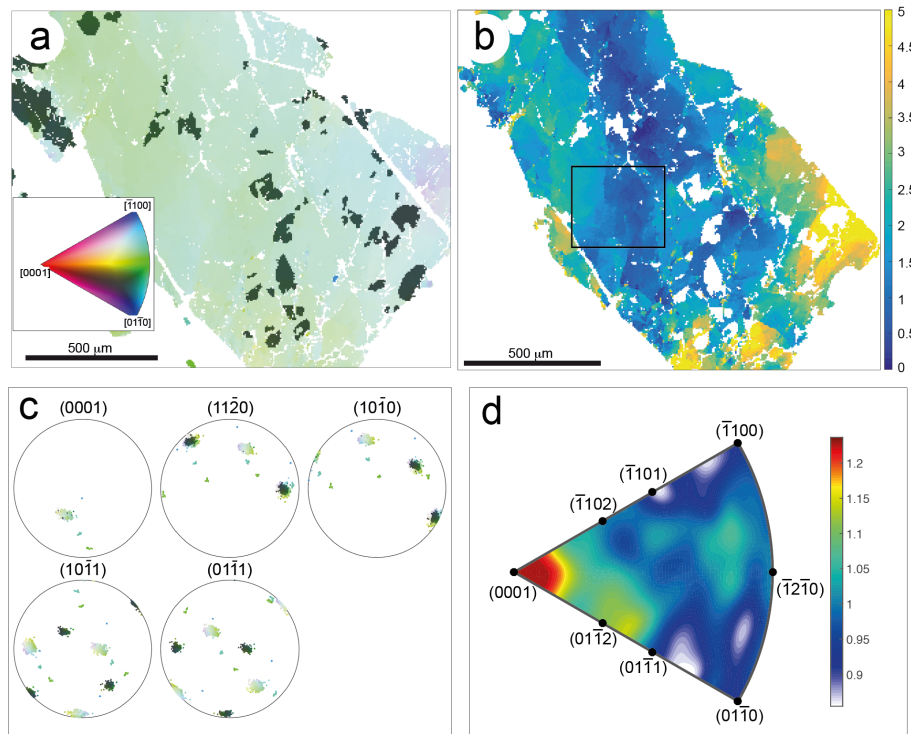
Figure 5. EBSD measurements on the quartz grain shown in Fig. 4. **(a)** Crystallographic orientation map measured using EBSD. The inverse pole figure (IPF) coloring indicates the orientation of each pixel relative to the horizontal axis of the map. The dark green patches correspond to Dauphiné twinned domains defined by a 60° rotation around the [0001] axis. **(b)** Misorientation map relative to the mean orientation of the quartz grain (excluding Dauphiné twins) with misorientations up to 5°. The rectangle indicates the area studied in Fig. 10. **(c)** Pole figures of the principal crystallographic axes of quartz using the same color code as in panel **(a)**. Upper-hemisphere projection. **(d)** Inverse pole figure of rotation axes that correspond to misorientations between 0.5 and 5°. Color scale: multiple of uniform distribution.

crofracture geometry. Superimposed smaller misorientation domains are roughly elongated parallel to but cross-cut by the microfractures. The misorientation angle relative to the mean reaches up to 10° in this area (Fig. 8b) compared to the 5° misorientation in the mildly microfractured quartz mapped in Fig. 5b. Rotation axis of subgrain boundaries showing > 0.5° misorientation is again close to [0001] (Fig. 8d). However, pole figures (Fig. 8c) do not show significant dispersion of crystallographic axes around [0001]. The three components of rotation (Rx, Ry and Rz) were calculated using the EBSD data and the LaueTools package (Fig. 9; see Sect. S1 in the Supplement for mathematical transformations applied to the EBSD data in order to pass the orientation matrices and map point positions into the LaueTools sample reference frame). They indicate that neighboring fragments did not rotate greatly relative to each other (2 to 5°) during fragmentation. Actually, the Rx component (max. 30 mrad or 1.72°) is slightly lower than Ry (max. 64 mrad or 3.67°) and Rz (max. 90 mrad or 5.15°).

6   Elastic strain and residual stress

In order to characterize the small misorientation domains and the damage related to microfracturing, a small area of the representative quartz grain studied in Figs. 4 and 5 (see location in Figs. 4b and 5b) was investigated in detail using EBSD and X-ray Laue microdiffraction.

6.1   Orientation map

A high-resolution EBSD map was performed with a 0.5 μm step and misorientation to the mean orientation was calculated (Fig. 10b). As already observed in Fig. 4c and d, two types of intracrystalline deformation features are observed: (i) large 50 to 100 μm wide subgrains limited by sharp straight or slightly curved subgrain boundaries (Fig. 10b) with 0.5 to 1° misorientation indicated by large steps on the misorientation profile (Fig. 10c) and (ii) small elongated subgrains within the large ones, NNE–SSW orientated and showing less than 0.3° short wavelength misorientations (Figs. 10c and S4). This misorientation angle is comparable to the accuracy of the EBSD measurements performed with the CrystalProbe. However, as the small elongated subgrains coincide with the healed short microfractures or the align-
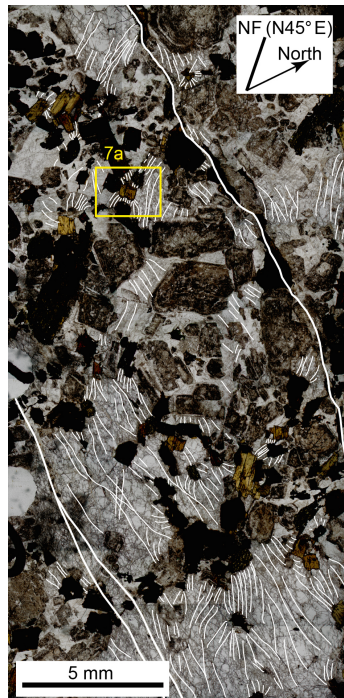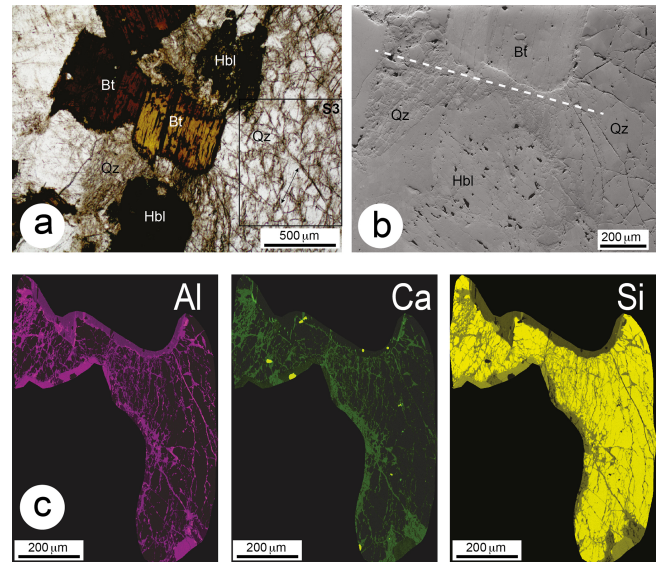
Figure 6. Schematic drawing of the NOJ220 thin section showing an array of numerous microfractures (thin white lines) joining one biotite or hornblende to another on the entire thin section width. The thicker white lines indicate breccia-like laumontite veins (see Fig. 3a for location). The yellow rectangle localizes the area studied in Figs. 7 and 8. The orientation of the thin section is inverse and indicated in the top left box (NF: Nojima fault).

Figure 7. Microstructures in the area shown in Fig. 3a. **(a)** Quartz grains squeezed between a biotite (Bt) and a hornblende (Hbl) and displaying intensive microfracturing. The small black arrow on the right indicates the preferred orientation of the alignments of tiny fluid inclusions in quartz (compare with Fig. 4a). **(b)** Forward-scattered electron image of the same area. The slightly different gray levels in quartz are due to different crystallographic orientations. The white dashed line locates the transect on which a 30 % dilatancy has been measured. **(c)** Compositional maps of the same area for Si, Ca and Al showing the laumontite-filled veins.

ments of tiny fluid inclusions (arrows in Fig. 10a and b), they are believed to be significant even if their misorientation is very small ($< 0.2°$; see Fig. S4). Misorientation axes corresponding to some of these subgrains have been determined (Fig. 10d) and are close to [01-11] or [01-12].

The same area has then been analyzed using X-ray Laue microdiffraction. A high-definition map with a 2.5 µm step (89 lines, 101 columns, 8989 images) was constructed in the 250×220 µm^2 zone. In this area, the relative simplicity of the Laue images (low number of subgrains within the analyzed volume) allows the measurement of the orientation and local deviatoric distortion of the quartz unit cell with a good precision (~ 0.1 mrad). The crystallographic orientation was determined at each point of the map and the rotations Rx, Ry and Rz of the crystal lattice around the x, y and z axes (sample referential; see Fig. 2) relative to the average orientation matrix were calculated (Fig. 11a; see Appendix A1 for the details of calculation and methods of data filtering).

The spatial and angular resolutions obtained with X-ray Laue microdiffraction are lower and higher, respectively, than those obtained with EBSD. However, these two techniques sample different regions as EBSD samples the surface and X-ray Laue microdiffraction a volume of

$1 \times 1 \times 100$ µm^3, respectively (see Sect. 3). There is a good correlation between the domains indicated by Rx, Ry and Rz rotations calculated with the LaueTools package applied on X-ray Laue microdiffraction data (Fig. 11a) and on EBSD data (Fig. 11b). The subgrain boundaries correspond to the misorientation maps and the misorientation angles measured with the two methods are comparable (Fig. 11a and b). These maps also indicate that Ry misorientations are larger than Rz and Rx for both techniques. Moreover, the Ry map highlights the small elongated subgrains parallel to the healed short microfractures or the alignments of tiny fluid inclusions.

6.2 Lattice distortion – elastic strain

The deviatoric elastic strain measurement performed by X-ray microdiffraction is based on the slight distortion of the measured Laue pattern compared to the pattern of an undeformed crystal of the same orientation, i.e., the angular distances between spots of the Laue patterns in the deformed crystal are compared to those of an undeformed reference pattern. The data have been filtered using two estimators of the quality of the Laue pattern refinement (number of spots and average distance between experimental and reference pattern spots; see Appendix A1 for explanation). It is pos-
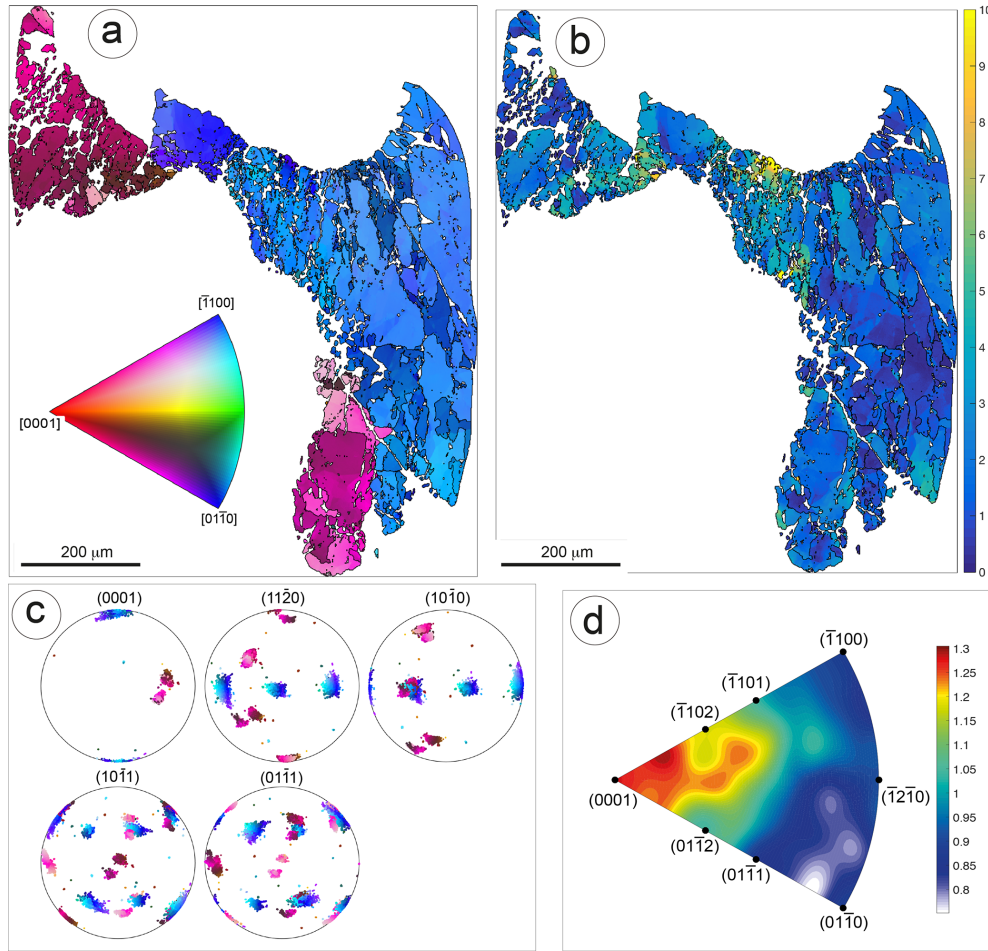
Figure 8. EBSD measurements on the quartz grains shown in Fig. 7. **(a)** Orientation map: the color scale indicates the minimum angle between each pixel and the reference orientation defined by (0, 0, 0) Euler angles. **(b)** Misorientation map relative to the mean orientation of each quartz grain with misorientations up to 10°. **(c)** Pole figures of the principal crystallographic axes of the three quartz grains using the same color code as in panel **(a)**. Upper-hemisphere projection. **(d)** Inverse pole figure of rotation axes that correspond to misorientations between 0.5 and 10°. Color scale: multiple of uniform distribution.

sible to calculate the six main components of the deviatoric elastic strain tensor (ε_{XX}, ε_{YY}, ε_{ZZ}, ε_{YZ}, ε_{XZ}, ε_{XY} with $\varepsilon_{XX} + \varepsilon_{YY} + \varepsilon_{ZZ} = 0$) at each point of the map (Fig. S5). Values of equivalent strain may be calculated from the strain tensor

$$\varepsilon_{\text{eq}} = \frac{2}{3}\left[(\varepsilon_{XX} - \varepsilon_{YY})^2 + (\varepsilon_{YY} - \varepsilon_{ZZ})^2 + (\varepsilon_{ZZ} - \varepsilon_{XX})^2 \right.$$
$$\left. + 6\left(\varepsilon_{XY}^2 + \varepsilon_{XZ}^2 + \varepsilon_{YZ}^2\right)\right]^{\frac{1}{2}} \tag{1}$$

and are reported without filtering (Fig. 12a) or after filtering (Fig. 12b). Equivalent strain and the components of the elastic strain tensor (Fig. S5) are roughly correlated with the microstructures revealed by EBSD (subgrain boundaries; see Fig. 10b), with the Rx, Ry, and Rz maps (Fig. 11) and with microfractures as well. However, some domains with no important misorientation or subgrains such as the upper left

corner on the map (Fig. 11) display important elastic strain (more than 2.5×10^{-3}, Fig. 12).

The distribution histograms of the equivalent strain value at each point of the map is given in Fig. 13a. Without filtering, equivalent strain varies up to more than 2.5×10^{-3}, but the highest values ($> 2.5 \times 10^{-3}$) are removed by filtering. Nevertheless, the mean equivalent strain after filtering is still at 0.96×10^{-3}.

6.3 Residual stresses

The distortion of the crystal lattice measured above is purely elastic; thus the residual deviatoric stress tensor may be calculated at each point of the map by applying Hooke's law:

$$\sigma_{ij} = C_{ijkl}\varepsilon_{kl}, \tag{2}$$

where σ is the stress, ε_{kl} the elastic strain and C_{ijkl} the elastic coefficients for α quartz as determined by Ogi et al. (2006) at
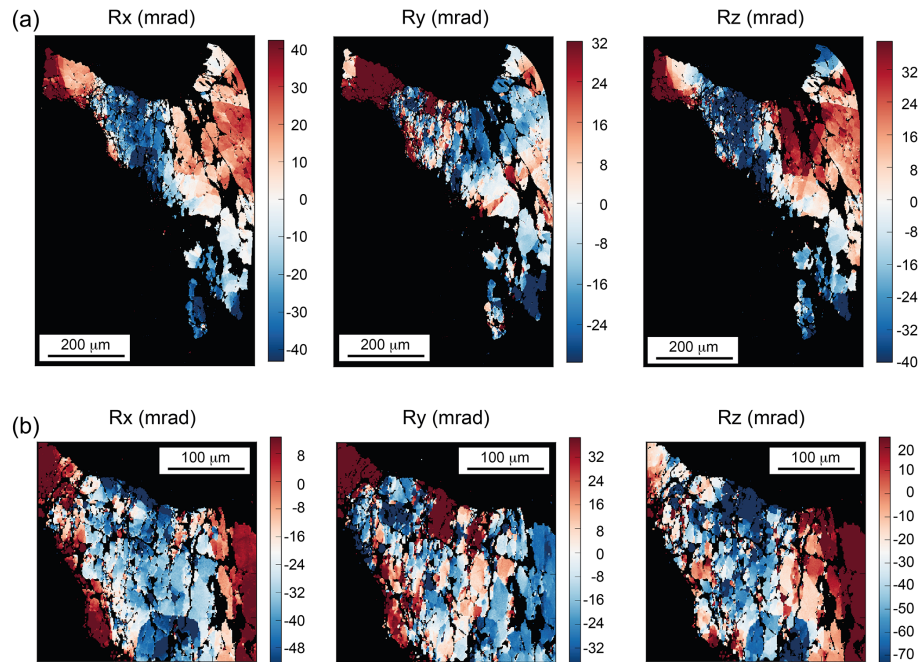
Figure 9. Maps of the Rx, Ry and Rz rotations of the crystal lattice around the x, y and z axes (sample referential), in the region explored in Fig. 8. Rx, Ry and Rz were calculated with LaueTools from the EBSD data of Fig. 8. The x, y map positions and the Euler angles of the EBSD file were first transformed in order to adapt to the LaueTools (LT) reference frames. The corresponding transformations are described in Sect. S1. Histograms of orientation matrix components were then built for different rectangular regions in the map of Fig. 8a in order to identify the frequency peaks associated with the blue crystallite in the center of the map and to define the thresholds for selecting the map points belonging to this crystallite according to their crystallographic orientation. In Fig. 9a, all the non-black pixels have their $\boldsymbol{a}^*$ vector within less than 245 mrad (14°) of the x axis. These pixels were used to calculate the mean orientation matrix of the crystallite (used as the zero for rotations). The twinned regions appear in black, i.e., they were excluded from the crystallite. **(a)** Rotation components for the right part of Fig. 8a. **(b)** Zoom on the top-center area of Fig. 8a. Scales in milliradians differ (in amplitude and offset) among the different maps in order to enhance the contrast for each rotation component.

30 °C. Because of the proportionality between elastic strain and stress, the maps representing the components of the residual deviatoric stress tensor are similar to the map of the elastic strain components.

The von Mises (or equivalent) stress is a useful scalar to compare the state of stress at different locations in a crystal. As for equivalent strain, the von Mises stress was calculated at each point of the map following the equation

$$\sigma_{eq} = \left(\frac{1}{2} \left((\sigma_{xx} - \sigma_{yy})^2 + (\sigma_{yy} - \sigma_{zz})^2 + (\sigma_{xx} - \sigma_{zz})^2 \right. \right.$$
$$\left. \left. + 6 \left((\sigma_{yz})^2 + (\sigma_{xz})^2 + (\sigma_{xy})^2 \right) \right) \right)^{\frac{1}{2}} \quad (3)$$

and reported as a distribution histogram (Fig. 13b). The distribution of the filtered von Mises stress displays a modal value at 100 MPa for a mean at 141 MPa.

As pointed out by the anonymous referee, the deviatoric stress and von Mises stress obtained from deviatoric strain measurements are only approximate due to the trigonal structure of the quartz, which creates coupling between deviatoric strain (stress) and expansion stress (strain). The largest error due to this approximation is 24 MPa (see Sect. S2 for an

evaluation of the error). For simplicity, the term "von Mises stress" is used in this paper to mean the pseudo von Mises stress calculated from deviatoric strain.

7 Interpretation and discussion

The NOJ220 sample studied in this paper is located 51.3 m from the main Nojima fault, which is outside the damage fault zone determined on the basis of studies of the drill core samples (Ohtani et al., 2000a; Tanaka et al., 2001). Deformation microstructures corresponding to a low strain are nevertheless present in the thin section. We now discuss the observed microstructures in terms of stress and strain rate, i.e., their time of formation in relation with a seismic rupture (Fig. 14), and their significance in the development of the damage zone around the Nojima fault.

7.1 Laumontite-filled veins

Two types of veins or microfractures have been defined in the NOJ220 sample. The fact that all of them are sealed by laumontite clearly indicates that they accompanied the first
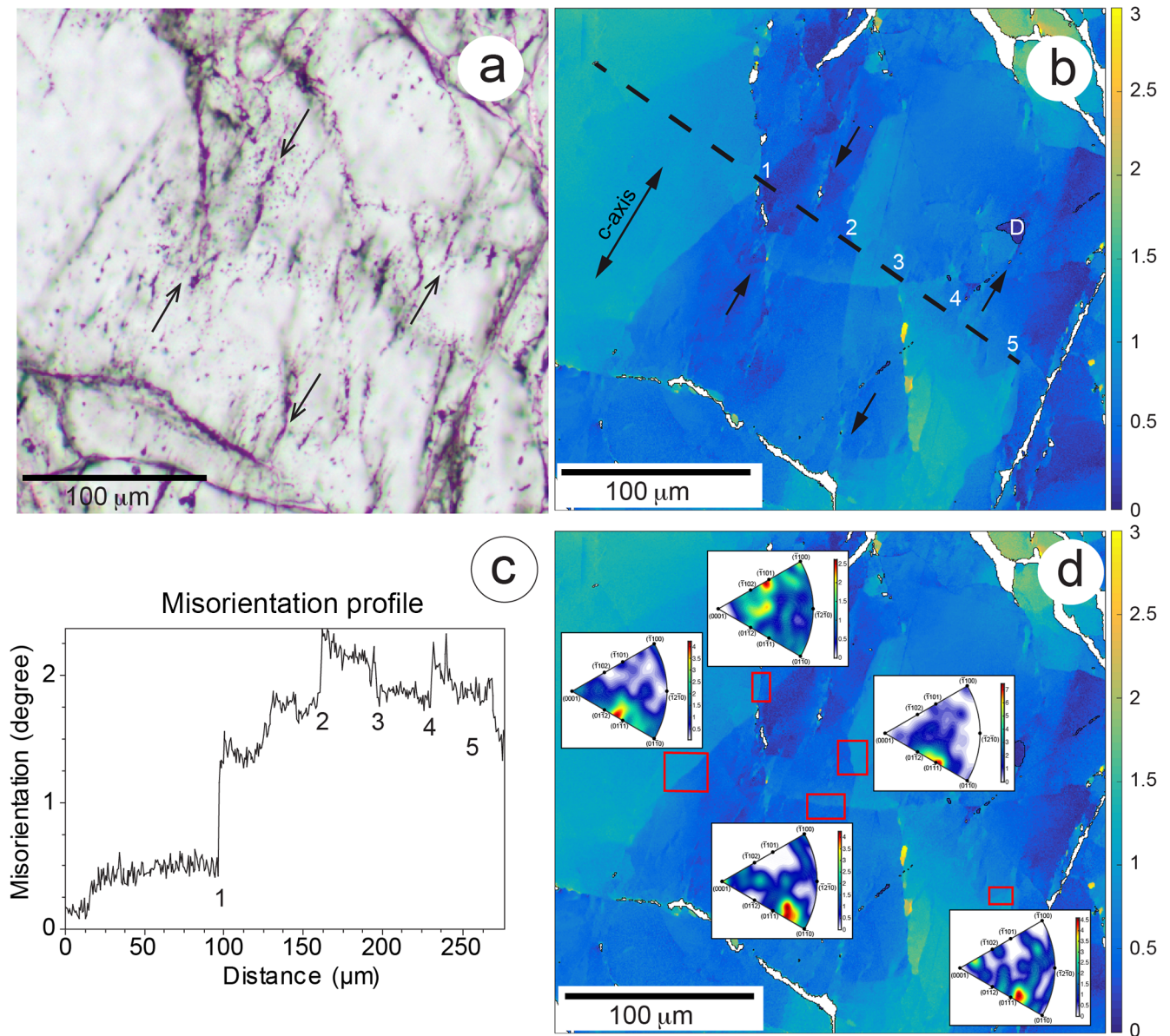
Figure 10. EBSD measurements on the area shown in Fig. 4b. **(a)** Optical microphotograph showing the short microfractures (thin arrows) and alignments of tiny fluid inclusions. **(b)** Map of misorientation of pixels relative to the mean orientation of the grain obtained by EBSD. The small dark domain (*D*) is a Dauphiné twinned domain. The projection of the [0001] axis on the thin section plane is shown by the double black arrow. The short black arrows indicate the well-orientated small elongated domains that could correspond to the short wavelength variations among subgrain boundaries or steps indicated as 1 to 5 in the profile drawn in panel **(b)**. **(c)** Misorientation profile along the dashed line shown in panel **(b)**. **(d)** Misorientation axes calculated for small areas across subgrain boundaries (red rectangles).

period of seismic activity on the Nojima fault (Boullier et al., 2004a) around 56 Ma (Murakami and Tagami, 2004). As already pointed out, the laumontite stability field in the 100–300 MPa pressure range (Cho et al., 1987) constrains the depth of formation of these veins at 3.7–11.1 km of depth. The E–W orientation of the two types of laumontite veins is not consistent with the left-lateral wrenching kinematics of the Nojima fault during its first period of activity. This point will be discussed later.

In the E–W striking breccia-like veins, the large and angular fragments of minerals suggest the absence of attrition. The fragments were transported away from their source locality by fluid advection in the fractures at least before the complete sealing by laumontite. Thus, the opening of one breccia-like vein corresponds to a single transient high-permeability stage in the Nojima fault vicinity and is interpreted to have occurred during a single seismic event. Fracture opening has induced post-seismic circulation of a hot

(a) X-ray Laue microdiffraction data

(b) EBSD data analyzed with LaueTools
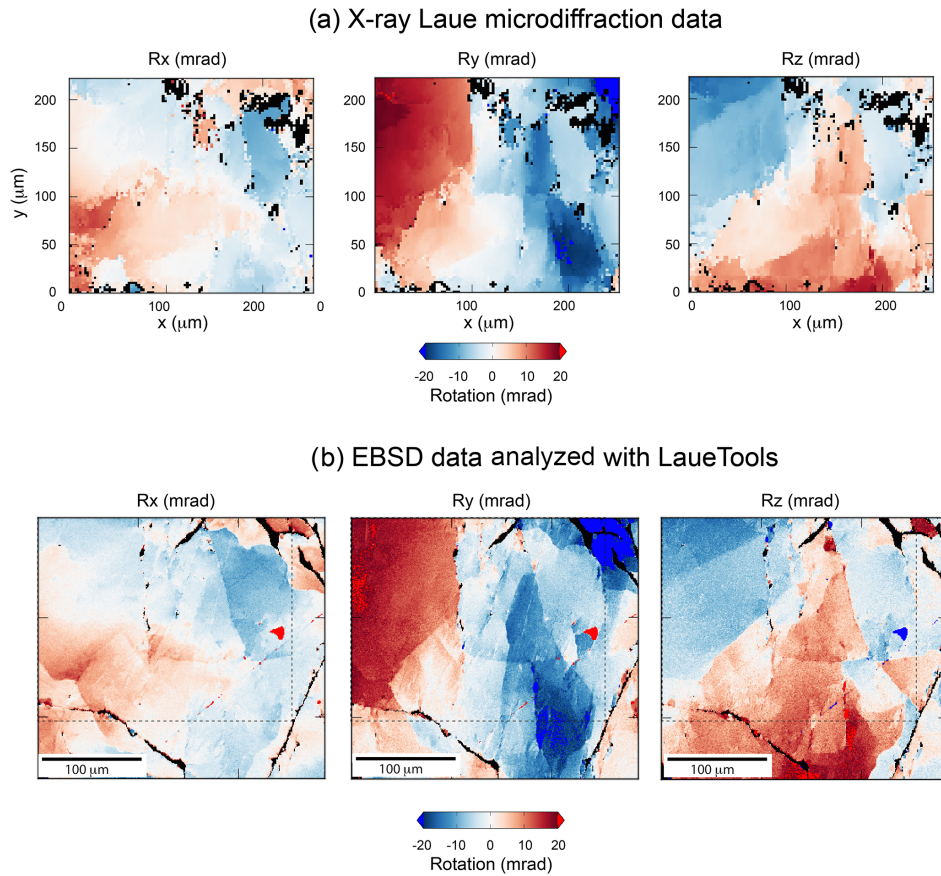
Figure 11. Maps of the Rx, Ry and Rz rotations of the crystal lattice around the x, y and z axes (sample referential) relative to the average orientation in each map in the small area described in Fig. 10 and calculated using LaueTools. **(a)** Rotations calculated from the X-ray Laue microdiffraction data. **(b)** Rotations calculated from EBSD data. The dashed line indicates the area investigated using X-ray Laue microdiffraction. See Sect. S1 for mathematical transformations applied to the EBSD data in order to pass the orientation matrices and map point positions into the LaueTools sample reference frame.
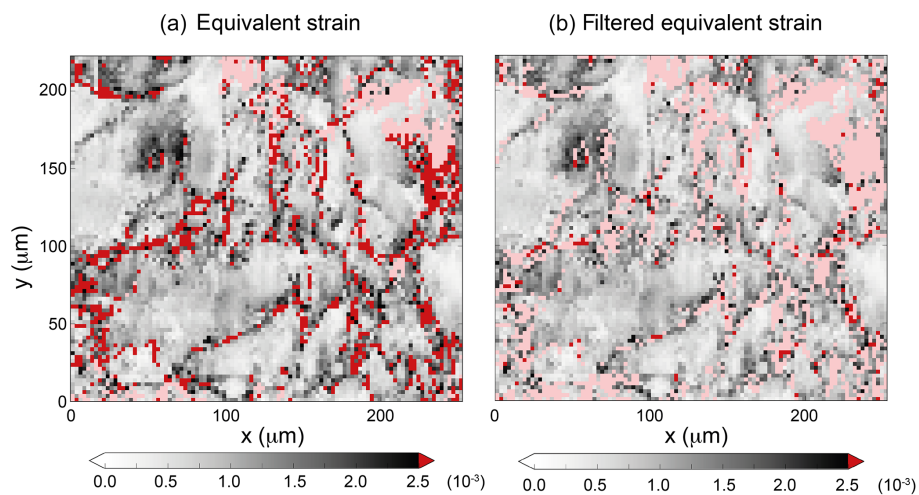

Figure 12. Maps of the equivalent strain (see Eq. 1 in the main text) measured from the distortion between the Laue pattern compared to the theoretical pattern of an undeformed crystal of the same orientation. **(a)** Unfiltered data. Undetermined points are pink. **(b)** Same data after filtering; same scale as in **(a)**; filtered points in pink (7259 images remaining over 8989). Note that filtering eliminates almost all the points showing an equivalent strain greater than 2.5×10^{-3}.
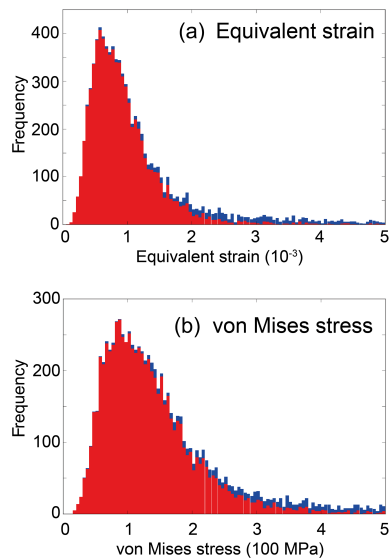
Figure 13. Distribution histograms of equivalent strain **(a)** and residual or von Mises stress values **(b)** without filtering (blue) or with filtering (red).

fluid coming from greater depths and crystallizing laumontite during cooling (Fig. 14). Two breccia-like veins are observed in the studied thin section. Either these two veins were formed during the same seismic event or they were formed during two different but similar earthquakes.

The significance of the second type of veins is not so clear. The morphology of the laumontite prisms and their orientation with respect to the vein walls confirm that they are mode I opening fractures and suggest equal rates of vein opening and laumontite growth by comparison with numerical modeling of vein opening and sealing (Hilgers et al., 2001). These veins are E–W orientated and on average parallel to (or branched on) the breccia-like laumontite-filled veins and thus are probably associated with them. However, they do not contain mineral fragments; this may be due either to their smaller thickness preventing the transport of fragments by advecting fluid or to a slower rate of fracture opening. The type 2 veins, and especially the dense array illustrated in Fig. 6, are also very similar in shape to the experimental fractures described by Aben et al. (2016). These authors have performed successive high-strain-rate loadings (180 to 90 s^{-1}) on granitic cylinders using Hopkinson bars below the pulverization threshold in order to simulate successive seismic events. The numerous fractures created in these experiments run roughly parallel to the loading direction and show only dilation and no shear (Aben et al., 2016). The quartz grain described in the Fig. 7 and displaying fractures radiating in a Hertzian pattern may also be compared to quartz grains in damaged sandstones along the San Andreas Fault (Dor et al., 2009). By analogy, the opening of type 2 laumontite veins is tentatively attributed to the coseismic or dynamic stage (Fig. 14), although their orientation is more dif-
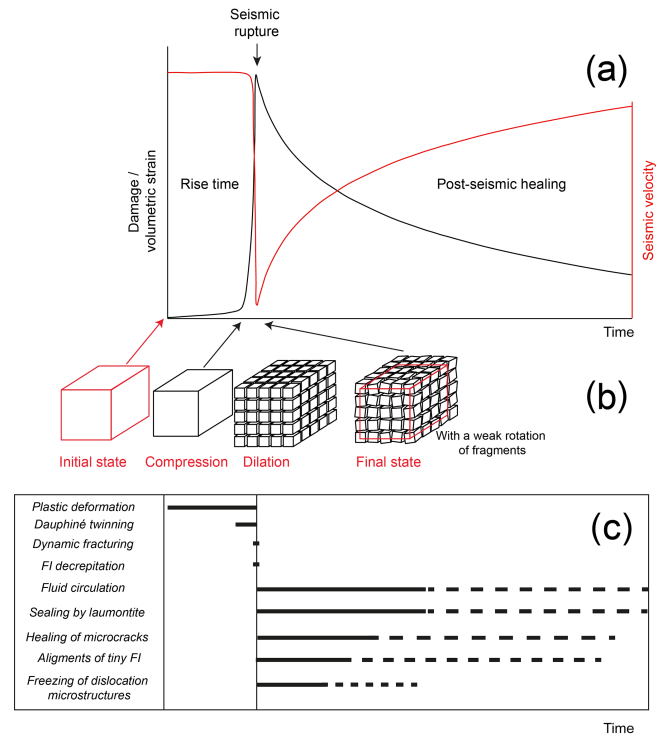
Figure 14. Schematic interpretation showing the relationships between one characteristic earthquake and time of formation of the different microstructures observed in the NOJ220 sample. **(a)** Variations in volumetric strain or damage versus time before and after a rupture. The red curve is drawn from the relative velocity changes observed by Brenguier et al. (2008) near Parkfield (California) for 3 years after the M6 28 September 2004 Parkfield earthquake. **(b)** Image inspired by Reches and Dewers (2005) explaining the effect of a rupture front propagating on a fault. Successive compression and dilation (or dilation and compression) leads to fragmentation. **(c)** Time and duration of formation of microstructures relative to the seismic rupture.

ficult to interpret (E–W-striking veins versus 50° N-striking Nojima fault). Do these veins represent one or several seismic events? Following Aben et al. (2016) additional loading led to the growth of new fractures rather than failure on the already created fractures, resulting in homogeneously distributed fractures within the sample. Therefore, the sum of the veins, either breccia-like or mode I, that are observed in the NOJ220 sample may correspond either to several similar "mild" seismic events characterized by similar loading conditions (characteristic earthquakes) or to the propagation of a single seismic rupture. If a single event is favored for the formation of the fracture array shown in Fig. 6, it is probable that all the laumontite veins observed in the thin section formed during several similar earthquakes. Whatever the interpretation, the consequence of coseismic fracturing is a fast and transient increase in the permeability, allowing circulation of hot advecting fluids and sealing of fractures by laumontite (Fig. 14).

7.2 Microfractures and alignments of tiny fluid inclusions in quartz

What are the relationships between the formation of microfractures and the alignments of tiny fluid inclusions? As described above, the alignments of tiny fluid inclusions are well orientated at the sample scale (Fig. S1), independent of the orientation of the host quartz crystal, and are parallel to the Nojima fault. Therefore, we may infer that quartz behaves as an isotropic material during the dispersion of large fluid inclusions into tiny ones and that this phenomenon is related to the macroscopic tectonic loading. Small intragranular microfractures and alignments of tiny fluid inclusions have the same cathodoluminescence signatures (Figs. S2 and S3), identical to those of quartz in the vicinity of laumontite-filled veins. Consequently, both microstructures are spatially linked and are interpreted to have formed simultaneously at a geological timescale. The alignments of tiny fluid inclusions are associated with a small ($< 0.3°$) lattice misorientation visible on the EBSD map in Fig. 10b, indicating that they result from a combination of brittle and plastic deformation of the quartz lattice. By comparison with experimental studies in which fluid-inclusion-rich quartz is submitted to a 10^{-8} to 5×10^{-9} strain rate under 200–600 MPa at 200–800 °C in a Griggs apparatus (Tarantola et al., 2010) and with similar natural fluid inclusions (Diamond and Tarantola, 2015), alignments of tiny fluid inclusions are tentatively interpreted as large decrepitated former fluid inclusions in an anisotropic stress regime. They are perpendicular to the principal stress in experiments (Tarantola et al., 2010) or to the regional compression in natural samples (Diamond and Tarantola, 2015). Recent similar experiments have confirmed this observation (Stünitz et al., 2017).

Decrepitation or dispersion of the large former fluid inclusions was probably accompanied by contamination of the primary fluid in the inclusion by the laumontite-bearing fluid circulating in microfractures during the first period of seismic activity of the Nojima fault. Decrepitation was then followed by a stress-driven dissolution–diffusion–precipitation mechanism leading to fracture healing and formation of neonate fluid inclusions. It is believed that decrepitation of large fluid inclusions and microfracturing occurred during the seismic stage, and that healing of alignments of tiny fluid inclusions took place during the post-seismic stage. If healing is a slow mechanism at the experimental timescale (several days or weeks; Pêcher, 1981; Brantley, 1992; Tarantola et al., 2010), it may contribute to the relatively fast post-seismic strengthening and seismic velocity recovery observed along active faults during the few months after an earthquake (Brenguier et al., 2008).

In their experiments, Tarantola et al. (2010) and Stünitz et al. (2017) have demonstrated that alignments of tiny fluid inclusions form in a plane perpendicular to the maximum compressive stress. Even more, the direction of the alignments of tiny fluid inclusions in the NOJ220 sample is roughly parallel to kink bands in biotite (Fig. S1), which themselves form perpendicular to the maximum compressive stress (Cummings, 1965). This suggests that maximum compressive stress was at a high angle to the Nojima fault in the crust when the alignments of tiny fluid inclusions and kinks in biotite formed. This configuration of stress is consistent with that measured by Ikeda et al. (2001) only 1.5 years after the Kobe earthquake and characterized by the maximum stress being perpendicular to the Nojima fault trace. The same configuration has been measured near the San Andreas Fault at Cajon Pass, California (Shamir and Zoback, 1992).

7.3 Plastic deformation of quartz

Deformation microstructures observed in quartz in the NOJ220 sample give information on stress and strain rate. The maps of crystallographic orientation of quartz in the NOJ220 sample show Dauphiné twins and misorientation domains or subgrains that are indicative of a plastic deformation. The cross-cutting relationships between subgrain boundaries indicate that the large subgrains formed before the small ones and may be attributed to the cooling history of the granodiorite as frequently observed in granitic rocks (Nédélec and Bouchez, 2011). Subgrain size is related to stress during plastic deformation (Sherby et al., 1977) by the equation $\lambda = Ab(\sigma/E)^{-1}$, where λ is the subgrain size, A is a dimensionless constant of proportionality which is approximately equal to 4 for many materials, b is the Burgers vector length, σ is stress, and E is Young's modulus. Therefore, a regime of increasing stress would result in reducing subgrain sizes nested in larger subgrains during plastic deformation as observed in the NOJ220 sample. Small subgrains or short wavelength misorientations are classically observed in rocks naturally deformed at low temperature (see for example Derez et al., 2015) or experimentally deformed at high temperature but high stress and strain rates (Trepmann, 2009; Trepmann and Stöckert, 2013; Trepmann et al., 2017). The small subgrains are elongated parallel to the microfractures and alignments of tiny fluid inclusions suggesting that the three types of microstructures are issued from the same high-stress deformation event.

Misorientation axes of the small subgrains have been determined in the quartz grain mapped using EBSD and were identified as [0001] (Figs. 5 and 8) but were close to [01-11] or [01-12] in the small area mapped with a high resolution (Fig. 10). They could give information on the active glide systems and on deformation conditions provided that their orientation and nature (tilt or twist boundary) are known (Lloyd, 2004). Unfortunately, we did not perform transmission electron microscopy observations to determine dislocation microstructures in the NOJ220 sample. However, more important than the activated glide systems is the small size of the elongated subgrains, the absence of bulging at grain boundaries and the presence of microfractures that are all together characteristic of a deformation occurring in the

semi-brittle faulting regime of quartz as defined by Hirth and Tullis (1994) and Tullis (2002) on the basis of experiments at high strain rate and low temperature ($> 10^{-6}\,\mathrm{s}^{-1}$, $< 700\,°\mathrm{C}$). Extrapolation of experimental results to natural conditions ($T < 300\,°\mathrm{C}$ as shown by the presence of laumontite) indicates a strain rate higher than $10^{-5}\,\mathrm{s}^{-1}$ (Tullis, 2002). The absence of recrystallization, the small angle of misorientation ($< 5°$) and the 5 % maximum shortening of biotite cleavages indicate a low finite strain. High strain rate and low strain combined together suggest that microstructures originated during a short-duration transient deformation event such as a seismic rupture.

Because of the emergence of new techniques to measure complete crystallographic orientation of quartz, Dauphiné twinning is now recognized in naturally deformed quartz-bearing rocks. Dauphiné twins may form in nature in a wide range of strain rate conditions from mylonitic quartzite (Lloyd, 2000, 2004; Pehl and Wenk, 2005; Menegon et al., 2011) to meteoritic impact (Wenk et al., 2005, 2011). Experimental studies were performed to investigate the influence of stress and temperature on Dauphiné twinning and have shown that it initiates at 50–100 MPa at 500 °C and that activation twinning is temperature dependent (Wenk et al., 2006). Recently, Wenk et al. (2011) have described Dauphiné twins in quartz from shock experiments, impact structures, pseudotachylites, and fault breccias and conclude that these microstructures are diagnostic of high and transient seismic stresses. Thus, Dauphiné twins observed in quartz from the NOJ220 sample are tentatively attributed to one or possibly several episodes of high and transient seismic stresses. Twinning immediately preceded microfracturing and fragmentation as shown by cross-cutting relationships and their continuity in neighboring fragments in Figs. 5, 8, 9 and 10. Therefore, they are suggested to have formed during the rising stress time before the seismic rupture (Fig. 14).

7.4 Elastic strain and residual stress

Elastic strain in a quartz grain was measured with X-ray Laue microdiffraction, which allowed the calculation of the associated residual stress. What could be the origin of the residual stresses measured in quartz? How can such large residual stresses be preserved in a small volume for such a long time? One could argue that the residence of the sample at depth, i.e., under confinement, could have preserved the residual stresses in the quartz grains. In this case, these residual stresses should have been released during recovery by drilling and during sawing and thinning for thin section manufacturing. Therefore, confinement at depth is not a sufficient condition for preserving residual stresses. As discussed above, the studied quartz displays torsions and flexions of the quartz lattice, and subgrains or dislocation walls, which are attributed to dislocation creep under low temperature and high transient stress or strain rate as quoted above. It is known that a local stress field is associated with each

dislocation or dislocation wall because they correspond to a local elastic distortion of the crystallographic framework (Dieter, 1976; Nicolas and Poirier, 1976). Thus, we tentatively interpret the measured residual stresses as the sum of the local stresses attached to each dislocation or dislocation wall present in the quartz grain.

The maps of elastic strain indicate that the ε_{ZZ} component is slightly lower than the others. This could be interpreted as partially released elastic strain close to the free surface of the sample as suggested by Chen et al. (2015), who obtain the same results for a deformed quartz grain in the San Andreas Fault zone. However, as the studied NOJ220 thin section is horizontal, such a lower ε_{ZZ} strain component could also be related to the strike-slip tectonic environment of the Nojima fault during the Paleocene (Famin et al., 2014) corresponding to a vertical minimum compressive stress at that geological time. Supplementary X-ray microdiffraction studies on differently orientated thin sections are necessary to test these different interpretations.

The large gradients in elastic strain (xx, yy, and zz and yz, xz, and xy; Fig. S5) roughly match the microstructures (subgrain boundaries or microfractures). They correspond well to the threshold values of the two quality estimators and to the minimum values of diffracted intensity (see Appendix A1, Fig. A1). Thus, high elastic strain or distortion of the lattice may prevent a good fitting of the spot positions in the Laue pattern (the single-unit-cell model used to describe the pattern start to fail). Nevertheless, after filtering these points out, the mean value of von Mises stress remains high (141 MPa versus 223 MPa if not filtered) in the small $250 \times 220\,\mathrm{\mu m}^2$ studied area included in a single quartz grain (Fig. 13b).

We have only performed one scan in the NOJ220 sample using X ray microdiffraction and the representativity of this scan may be questioned. All quartz grains present in the NOJ220 sample display microstructures similar in style and intensity (microfracturing, dispersed fluid inclusions, short wave length misorientation, etc.) except along the array of very dense microfractures (Figs. 6 and 7) where these microstructures are more intense. Therefore, we believe that the residual stresses measured in such a small studied domain are representative of the whole sample and may represent a lower bound compared to the microfracture array quoted above.

Chen et al. (2015) obtained 130 MPa as a modal value in the histogram of von Mises stresses in a cataclastic quartz sample located 50 m away from the San Andreas Fault active zone in the SAFOD drill hole (California), and 200 MPa in a quartz located within the Vredefort meteoritic impact site in South Africa. Lower values (ca. 50 MPa) are obtained by Kunz et al. (2009) in the mylonitic (i.e., plastically deformed) Santa Rosa granite (California). Thus, our results (modal value in the histogram of von Mises stresses at 100 MPa) compare well to the values published by Chen et al. (2015) for quartz samples of the San Andreas Fault zone, although the NOJ220 studied sample is located outside of the damage zone of the Nojima fault.

As pointed out by Chen et al. (2015) the residual stresses have remained in the crystals for a very long time, as long as 2 Gyr in the case of the Vredefort impact. In the Nojima fault sample, elastic strain and residual stress have been preserved since 56 Ma, the age of the first period of seismic activity of the fault (Murakami and Tagami, 2004). They were not released during the uplift of the area from 3.7 to 11.1 km of depth (depth range of laumontite stability) to the near surface (< 1 km of depth), or during the Quaternary phase of seismic activity of the Nojima fault since 1.2 Ma. We believe that, in the present case, internal stresses could not be released after dynamic damage due to the very low temperature (< 300 °C) inhibiting reorganization of entangled dislocations and re-crystallization of quartz, the later being a potential marker of stress relaxation (Trepmann et al., 2017).

7.5 Implications for the development of the damage zone

As discussed above, we interpret the laumontite-filled veins, microfractures and fluid inclusion decrepitation as resulting from coseismic fracturing during characteristic earthquakes on the Nojima fault and we interpret the Dauphiné twinning and plastic deformation of quartz as high-strain-rate precursors of these dynamic events. These earthquakes left behind high von Mises stresses in the sample (modal value at 100 MPa, mean at 141 MPa). Earthquakes characterizing the first period of seismic activity along the Nojima fault were M6 to M7 magnitude events (Boullier et al., 2001). Their consequences may be compared to those of Californian earthquakes along the San Andreas Fault system where pulverized rocks were produced on the near surface within a 100 m wide zone (Dor et al., 2006; Rockwell et al., 2009). We believe that microstructures in the NOJ220 sample are representative of the incipient dynamic damage at depth induced by the propagation of seismic ruptures on the Nojima fault plane 51 m away from the studied sample. Imprints of this damage are resumed to a few fractures which are now sealed within laumontite and to residual stresses and microscale deformation structures in quartz. We postulate that successive seismic ruptures would cumulate residual stresses until exceeding the strength of the rock. While the strength of the undeformed and unaltered protolith of the Nojima fault is around 400 MPa at an effective confining pressure of 50 MPa, samples located at 14.5 and 5 m from the fault plane have a 200 and 150 MPa strength, respectively (Lockner et al., 2009). Thus, the residual stresses accumulated in the studied NOJ220 sample are already close to those of the damaged granodiorite and could have contributed to the softening of the fault wall and widening of the observed 45 m wide damage zone (Ohtani et al., 2000a; Tanaka et al., 2001).

As pointed out already, microstructures in the NOJ220 sample are very similar to the experimentally or naturally fragmented samples described by Aben et al. (2016), Dor et al. (2006, 2009), and Rockwell et al. (2009). We know that high confining pressure prevents complete pulverization but not fragmentation (Yuan et al., 2011). With confining pressure in the 100–300 MPa range when microstructures formed in the NOJ220 sample, the strain rate threshold was probably not attained and the granodiorite was microfractured, but not pulverized. The high stresses associated with the propagating seismic waves have induced elastic strain, which has not been completely released by the microfracturing process as shown by the matching with high-elastic-strain gradients and microfractures (Fig. S5). Today X-ray microdiffraction allows the measurement of the residual stresses remaining in the sample.

In their experiments, Aben et al. (2016) have shown that the pulverization threshold can be reduced by successive dynamic loadings at lower strain rate if the rock experiences dynamic fracturing during successive loadings. They show that each dynamic event leads to the growth of additional microfractures homogeneously distributed and that P-wave velocity decreases with an increasing amount of damage. P- and S-wave velocities have been measured on the GSJ Hirabayashi drill core samples by Zamora et al. (2000). At 204 m depth ($d_{fault} = 53.2$ m) mean V_P is $5320 \, \mathrm{m \, s^{-1}}$ on dry samples but falls to $4950 \, \mathrm{m \, s^{-1}}$ at 220 m depth ($d_{fault} = 51.3$ m) in the same core piece as the sample studied in this paper. Such a 7 % decrease in V_P velocity is another indicator for invisible damage in the sample whatever the dynamic or quasi-static origin of the damage. An important difference among experiments and natural fault zones is that fluid circulates during the interseismic period. Post-seismic hydrothermal healing of the dynamically created microfractures partially increases the strength of rocks as laumontite does in the Nojima samples (Fig. 14). Nevertheless, high residual stresses measured today by X-ray Laue microdiffraction may be considered a record of the propagating seismic waves along the Nojima fault.

As pointed out earlier, the E–W-orientated mode I laumontite veins are not consistent with the far-field tectonic setting of the fault, i.e., left-lateral wrench fault with N–S compression (Famin et al., 2014). If all the steps in the process of orienting the core sample and thin section are correct, these fractures do not correspond to quasi-static loading conditions. Only dynamic loading may explain them as induced by a sudden release of the accumulated tectonic compressive stresses. The elastic energy released this way may trigger extensional fractures and overshoot (Savage and Wood, 1971).

7.6 Implications on the dynamic damage mechanism

All the deformations described in this paper are interpreted as dynamically induced 51.3 m away from the Nojima fault. Do these observations provide information on the loading mechanism at the origin of the dynamic damage? Several processes have been recently proposed in the literature for explaining shallow damage zone pulverization (see review in Aben et al., 2017): dynamic compressive loading, dy-

namic tensile loading, fluid-assisted decompression, wrinkle-like pulses and supershear.

Experiments reproducing compressive loading using split-Hopkinson bars have produced microstructures qualitatively similar to those observed in the described sample. Thus, as suggested in this paper, compressive loading may be a good candidate for the dynamic damage on the Nojima fault. Experiments reproducing tensile loading are more difficult to realize (see review in Zhang and Zhao, 2014) and require specific sample shapes. These experiments reproduce simple fractures rather than pulverization (Zhang and Zhao, 2014). No microstructural analyses are available for comparing with the microstructures in the Nojima sample. Nevertheless, one has to keep in mind that dynamic tensile strength is lower than dynamic compressive strength (Zhang and Zhao, 2014) and that dynamic tensile loading should be easier to produce than dynamic compressive loading.

The fluid-assisted decompression model corresponds to hydrofracturing due to a sudden drop of fluid pressure in the rock. This mechanism is efficient in high permeability sedimentary rocks present in the subsurface. However, it appears highly unlikely in the case of the Nojima granodiorite, which has a very low permeability (10^{-20} to 10^{-21} m^2 under 50 MPa confining pressure; Lockner et al., 2009).

Considering the model of wrinkle-like pulses related to a bimaterial interface (Shi and Ben-Zion, 2006), it is not appropriate in the present case because both the footwall and hanging wall of the Nojima fault are constituted by the same granodiorite and the profile of physical properties of rocks across the fault is symmetrical (Lockner et al., 2009). Moreover, this model does not apply at great depth (> 3 km; Ben-Zion and Shi, 2005) where dynamic damage has been demonstrated to occur in the Nojima sample on the basis of laumontite in veins and microfractures.

The last model is the supershear, i.e., a rupture front propagating faster than the S-wave velocity (Bouchon et al., 2001) and the formation of a Mach cone (Rosakis et al., 2007). If supershear is mostly observed during high-magnitude earthquakes along simple large faults (Bouchon and Vallée, 2003), it may also occur along smaller linear segments (see review in Rosakis et al., 2007). It triggers damage laterally and also in depth (Bouchon and Karabulut, 2008). Thus, supershear could be invoked for inducing the dynamic damage at 51.3 m from the Nojima fault and at 3.7–11.1 km of depth.

To conclude, microstructures observed in the unique sample studied in this paper are interpreted as due to dynamic damage. However, suggesting a unique mechanism for explaining this dynamic damage would be overinterpreting the data. Additional microstructural observations on orientated samples across the Nojima fault, including samples outside and inside the damage zone, are necessary.

8 Conclusions

We have studied a core sample of granodiorite located 51.3 m from the Nojima fault (Japan) that was drilled after the Hyogo-ken Nanbu (Kobe) earthquake using EBSD and high-resolution X-ray Laue microdiffraction. Although macroscopically undeformed, the sample is pervasively microfractured and locally fragmented during the first stage of seismic activity along the Nojima fault. On the basis of the sealing hydrothermal laumontite, we are able to estimate that microfracturing occurred at 100–300 MPa confining pressure, i.e., at 3.7–11.1 km depth. EBSD mapping was used to characterize the crystallographic orientations and deformation microstructures in the sample, and X-ray Laue microdiffraction was used to measure elastic strain tensor in a quartz grain. Both methods give consistent results on the crystallographic orientation and show small and short wavelength misorientations associated with laumontite-sealed microfractures and alignments of tiny fluid inclusions. Deformation microstructures are symptomatic of the semi-brittle faulting regime in which low-temperature brittle and plastic deformation and stress-driven dissolution–precipitation processes occur conjointly.

Using Hooke's law, residual stresses and von Mises stresses are calculated from residual elastic strain measured using X-ray Laue microdiffraction. The von Mises stress distribution shows a modal value at 100 MPa, a value similar to that obtained on quartz located 50 m from the San Andreas Fault gouge. Such stress values are comparable to the peak strength of a damaged granodiorite from the damage zone around the Nojima fault indicating that, although apparently macroscopically undeformed, the sample is actually significantly damaged. The homogeneously distributed microfracturing of quartz is the microscopically visible imprint of this damage and suggests that high stresses were stored in the whole sample and not only concentrated on some crystal defects. It is proposed that the high residual stresses are the sum of the stress fields associated with dislocations and dislocation microstructures that were triggered by the dynamic damage related to the propagation of rupture fronts or seismic waves associated with M6 to M7 earthquakes during the Paleocene on the Nojima fault at a 3.7–11.1 km depth where the in situ confining pressure prevented pulverization. The high residual stresses and the deformation microstructures would have contributed to the widening of the fault zone with additional large earthquakes occurring on the Nojima fault.

Appendix A: X-ray Laue microdiffraction: method and parameters for the analysis of the series of Laue patterns

The methods for sample alignment and geometry calibration using the Laue pattern of a single Ge crystal were described in Ulrich et al. (2011). The four main stages of automated analysis of a Laue pattern (peak search, indexation, unit cell dimensions and orientation refinement) were described in Tamura (2014) and Robach et al. (2017), and also in the documentation of the LaueTools software.

For the quartz sample studied here, as described in Fig. 2c, two types of Laue patterns are encountered: type 1, which are single-crystal (one spot per HKL) Laue patterns, (about 70 % of the map) and type M, which is multiple closely oriented subgrain (several subspots per HKL) Laue patterns (about 30 % of the map). For type 1 points, the orientation and strain results are essentially "single-valued", i.e., are reproducible over a wide range of analysis parameters.

For type M points, a criterion needs to be arbitrarily chosen in order to decide which is the x, y position of a multispot or an asymmetrical spot. Indeed, although in theory a multigrain indexation procedure could be applied to the multispot Laue pattern, in order to individually index each subspot present on the beam path, in practice the corresponding code for closely spaced subspots is still unavailable. And at the stage of the display of the 2-D maps of strain or orientation, a decision needs to be made in any case, in order to select the individual subgrain or the mean grain to be displayed at each point. For type M points, results therefore widely vary depending on analysis parameters such as (i) the box size for the 2-D Gaussian fitting of the spots in the Peak Search stage, (ii) the angular tolerance for linking theoretical (undeformed reference crystal) and experimental spots at the SpotLink stage of the Indexation stage, and (iii) the threshold on pixel deviation for removing bad spots at the refinement stage.

In addition, there is a limit to the indexability of M points: when the groups of subspots are too wide, neighboring groups of subspots belonging to different HKLs start to intersect, and the number of indexed spots falls. For a type 1 point, the typical minimum distance between experimental spots is 17 pixels. This sets an upper limit on the width (in pixels) of the groups of subspots, above which the brute-force spot-linking process based on pixel distance only starts to produce ambiguous results (e.g., double-indexed experimental spots or double-linked theoretical spots).

An arbitrary choice was therefore needed for the analysis of the M points. Different indexation strategies were envisaged: a first approach is to try to select the subgrain closest to the surface, either by selecting the most intense subspot in each group (based on maximum pixel intensity or maximum integrated intensity), or by spot linking directly on the local orientation matrix determined with EBSD, taking advantage of the near-surface sensitivity of EBSD. Assuming that the angular accuracy of classical EBSD is around 0.3°

(5.2 mrad), the EBSD approach would only work if the sub-spots in each group were distant by more than 5 pixels. A second approach, the one chosen in this paper, is to average over all the subspots of the M point to create an average subgrain.

A1 "One-spot" analysis

Figure A1 illustrates the variations in the orientation maps produced by a change in the criterion used to calculate the x, y position of the experimental multispot (M point). Here a box of 201×201 pixels around the position $x\_pix, y\_pix = (1484, 1213)$ (0-222 spot of Fig. 2b) was extracted from the patterns. The positions xy_max and xy_fit of the spot were calculated by taking, for xy_max, the (integer) pixel position of the maximum of intensity, and for xy_fit, the (real) center position of the 1-D Gaussian curve obtained by fitting the intensity profile projected onto the y axis (respectively the x axis) for the x position (respectively the y position). The positions xy_max and xy_fit are mapped in Fig. A1a and b, respectively. This very simple one-spot analysis already allows the visualization of the subgrain structure inside the mapped region. Indeed, as a first approximation, the x (respectively y) position of the spot provides the crystal orientation in rotation around the y axis (Ry) (respectively Rx).

For M points, the choice of xy_max approximately selects the subgrain closest to the surface, assuming that its crystalline quality remains sufficient to always dominate with respect to deeper subgrains. The choice of xy_fit corresponds to building an "average grain" at each map point, with a diffraction-wise averaging, i.e., giving a larger weight to well-crystallized region, performed over the different subgrains present on the beam path.

The most remarkable difference between the (a) and (b) maps in Fig. A1 is the sharper aspect of the subgrain edges in panel (a). The averaging over depth in panel (b) therefore leads, as expected, to a degraded lateral resolution, especially when crossing non-vertical subgrain boundaries (with respect to the thin section). When comparing the subgrain structure between Fig. A1 and the EBSD misorientation maps of Fig. 11b, a closer similarity with panel (a) is observed, as expected for a criterion attempting to select the subgrain closest to the surface at each point.

A2 "N-spot" analysis

For the N-spot analysis of the Laue patterns, the xy_fit criterion was used (average subgrain for type M points). The subgrain edges in the final micro-Laue strain and orientation maps are therefore less sharp than in the EBSD maps.

Since the region mapped with X-rays was inside a single grain, the analysis of the series of Laue patterns was performed using a lightweight two-spot method to obtain the first guess orientation matrix. Indeed, the brute force index-
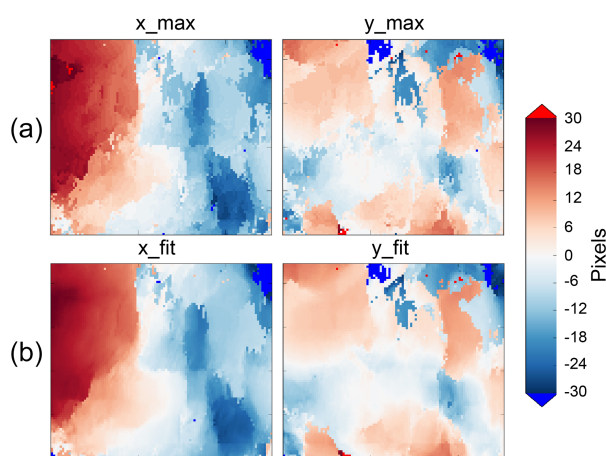
Figure A1. X-ray Laue microdiffraction: one-spot analysis. Maps of the x, y pixel position of the (0-222) spot, for two different methods of calculation of this position. The mean position was subtracted. **(a)** $xy\_$max (mean = 1476.43, 1211.59); **(b)** $xy\_$fit (mean = 1476.65, 1211.45). See text of Appendix A1 for definition. The difference between panels **(a)** and **(b)** is mostly visible for M-type points, where several closely spaced subgrains are present in the beam path.

ation of a quartz pattern is a CPU-consuming process due to the low symmetry of the crystal and the corresponding large number of possible theoretical angular distances between crystal planes, and a lighter procedure is preferable when processing a large number of images. Here classical indexation was applied to only one pattern, then two widely spaced low-Miller-index spots were selected: the (0-222) spot (spot 2) already analyzed in Fig. A1 and the (2-203) spot (spot 1) located around xypix = (659,1640). The interest of using low-index spots is that their first neighbor is comparatively far away (147 pixels for spot 2 and 131 pixels for spot 1): the risk of a spot with a different (HKL) entering the fixed 201×201 pixel wide box, due to the rotation of the crystal, is therefore limited. In practice, the highest spot displacement with respect to the box center (using $xy\_$fit) was 147 pixels for spot 2 and 57 pixels for spot 1. After excluding 11 bad points (over a total of 9077) the highest displacement for spot 2 was down to 58 pixels.

The two-spot analysis of the series of Laue patterns was performed using the $xy\_$fit positions for the spots. The resulting approximate orientation matrix (with an unstrained unit cell) was then used to perform a spot link (linking each theoretical spot to its nearest experimental neighbor) with the list of spots resulting from the peak-search procedure. The angular tolerance (among reciprocal lattice vectors) for the spot-linking process was $0.2°$.

Three estimators (npeaks, pixdev and intensity) of the local uncertainty on the shape–orientation of the unit cell were calculated with the LaueTools software (Fig. A2). The first estimator (npeaks) is the number of Laue spots used for the refinement of the local orientation and the distorted quartz unit cell. For map points with single sharp spots, a low npeaks gives good data quality (npeaks > 15; Fig. A2a). The minimal number of Laue spots needed for reaching the best accuracy on strain and orientation depends on the local crystalline quality: for type 1 points, 15 spots (npeaks = 15) are sufficient, while for type M points, 25 spots (npeaks = 25) are needed (Fig. A2a). The second estimator (pixdev, mean pixel deviation; Fig. A2b) is a measure of the fit quality and represents the mean distance between the experimental (as estimated from 2-D peak fitting on the detector image) and theoretical (as calculated from the refined orientation and distorted unit cell) x, y pixel positions of the Laue spots, averaged over the npeaks spots of the pattern. One pixel of pixdev typically gives an uncertainty of 10^{-3} mrad^{-1} on the strain–orientation components. The third estimator is the intensity and represents the average intensity of the 10 most intense spots of the Laue pattern of the grain (Fig. A2c). The spot intensity is the height (peak minus background) of the 2-D Gaussian curve used to fit the 2-D image in a box of 101×101 pixels around the spot center (boxsize = 50). The search for local maxima in the image (which produces the list of x, y pixel positions of spot centers) was performed using the convolution method, which proceeds as follows: first the image is convoluted with a 2-D Ricker wavelet function with a full width at half maximum of 3 pixels. This attributes all the Laue spots with a similar width. Thresholding is then applied on the convoluted image (thresholdConvolve = 3000), producing a first mask. The intense pixels in this mask are then grouped by clusters (blobs) based on a +-like connectivity criterion. The list of clusters is then reduced by applying a criterion of a minimal distance between two clusters (PixelNearRadius = 50 pixels). The list of remaining clusters is then reduced again by thresholding on the non-convoluted image, after subtracting the local background: Iraw - Ibackground > 50 (IntensityThreshold = 50) where Ibackground is the mean intensity on the frame of a box of 101×101 pixels (boxsize = 50) centered on the cluster center. The resulting mask is shown in Fig. A2d.

After the spot-link stage, the orientation and shape of the unit cell (strained orientation matrix) was refined once using the N indexed spots. Then the new pixel deviation (pixdev) between experimental and theoretical spots was calculated, and the refinement was run again after excluding spots with a pixdev larger than 3. This leads to the final values for npeaks and pixdev displayed in Fig. A2a and b. Figure A2d illustrates the filtering used for the final display of the elastic strain maps of Figs. 12 and S5.

Finally, we remark that more complete maps (in terms of number of points) can be obtained using only the two-spot analysis. Figure A3 shows the lattice rotation and strain results in this analysis, performed using $xy\_$max instead of $xy\_$fit. Only one scalar strain component is available in this analysis. The strain results obtained using $xy\_$fit are also shown.
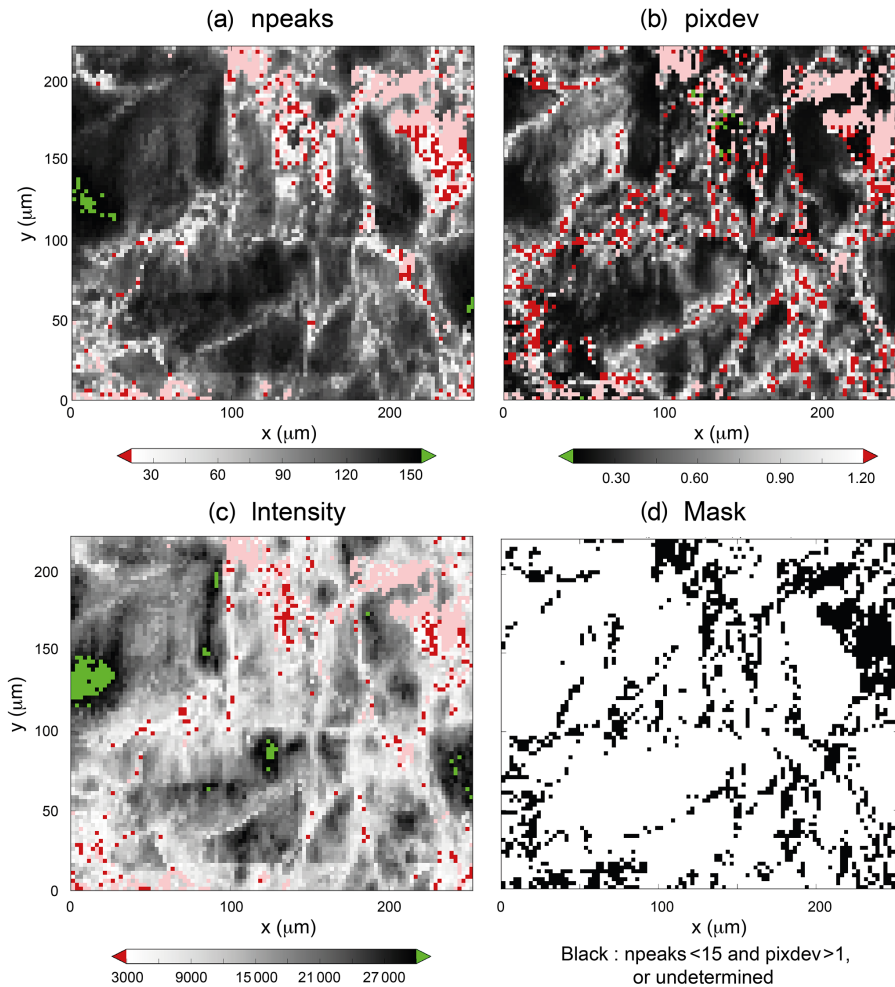
Figure A2. Maps of three estimators (npeaks, pixdev and intensity) of the local uncertainty on the shape–orientation of the unit cell, as calculated with the LaueTools software, and final mask used for removing bad data points (see explanations in the text). **(a)** Npeaks: number of Laue spots used for the refinement of the local orientation and deviatoric shape of the quartz unit cell. **(b)** Pixdev (mean pixel deviation): estimator of the fit quality. **(c)** Intensity: average intensity of the 10 most intense spots of the Laue pattern of the grain. **(d)** Mask used for removing bad data points from strain maps; black pixels have npeaks < 25 or pixdev > 1. Pink points in Fig. A2a, b and c are points where the spot link failed (missing points), and black points of the mask correspond to points either missing or with an npeaks below 25 or a mean pixdev above 1 pixel.

Appendix B: Method used for lifting the ambiguity between Dauphiné twins

For each quartz Laue pattern, two orientations rotated by 180° around the c axis (two Dauphiné twins) are compatible with the positions of the Laue spots. Hence an ambiguity arises in the spot indexation and the orientation matrix. Laue spot intensities need to be analyzed to lift this ambiguity (Chen et al., 2012). As pointed out by Dejoie et al. (2011), spots sorted according to theoretical structure factor are usually unsorted with respect to experimental intensities due to the strong influence of spot energy and theta diffraction angle on experimental intensity. In the case of quartz, both orientations lead to the same spot energy, which simplifies the analysis.

Most of the micro-Laue map in Fig. 11a is located inside a single twin. In the analysis, the small domain of twinned crystal (visible at the middle right in the corresponding EBSD map Fig. 11b) was treated as a domain of normal crystal, so it is invisible in the orientation maps. This domain becomes visible when plotting a map of box intensity (sum of pixel intensities over a box of 200×200 pixels centered on $x, y = 659, 1640$) of spot 2-203.

For the dominant twin of the micro-Laue map, the initial indexation provided by LaueTools was wrong (there was one chance over two, as only the spot positions were used). The ambiguity on the indexation was then lifted in the following manner.
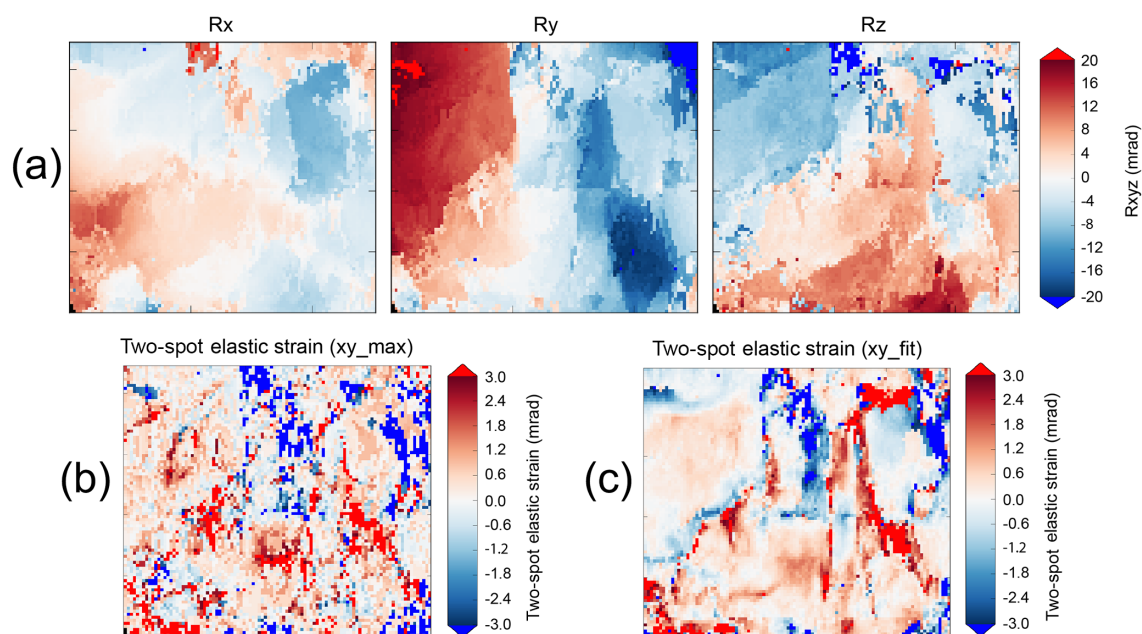
Figure A3. X-ray Laue microdiffraction: two-spot analysis, using the xy_max position of the (0-222) and (2-203) spots. **(a)** Lattice rotations with respect to the mean orientation, around the axes of the sample reference frame. **(b)** The two-spot elastic strain as measured from the angle between the reciprocal lattice vectors of the two spots (after subtracting the angle for unstrained quartz). **(c)** Same as panel **(b)** using xy_fit. High-strain map points (dalf > 5 mrad) are excluded when calculating the mean orientation matrix used in panel **(a)**.

The 196 indexed spots of the pattern were listed with their experimental intensity, the two possible values of the structure factor, the spot energy and the 2θ value. Structure factors were calculated using the cctbx web service (https://cci.lbl.gov/cctbx/structure_factors.html, last access: 19 April 2018; Grosse-Kunstleve et al., 2002) with the following parameters:

- lattice parameters: 4.913 4.913 5.404 90 90 120, space group 152, default convention for space group;

- atom coordinates in asymmetric unit: O 0.408 0.2881 0.23, Si 0.457 0 0.3333.

It was checked that the cctbx-calculated structure factors were consistent in terms of order with the results from the XMAS program of Tamura (2014): XMAS provides structure factors only indirectly via the possibility of thresholding on the structure factor in the simulated Laue pattern. The spots were then grouped according to both energy and 2θ, and the two structure factors were plotted versus intensity. The comparison between the two curves (normal and twin) showed a better match for the twin orientation. More precisely, the spots were grouped by intervals of ±0.5 keV for the energy and ±5° for the 2θ, with the intervals centered on the energy and 2θ of an existing spot, starting from the most intense spot. Going up to spot number 67, we obtained 40 cases with at least two spots in the group. Over these 40 cases, the twin crystal was favored in 16 cases (monotonous ascending curve for the twin, non-monotonous ascending curve for the normal), the normal crystal was favored in three cases (reverse criterion), and the ambiguity remained in 21 cases.

The Supplement related to this article is available online at https://doi.org/10.5194/se-9-505-2018-supplement.

References

Aben, F. M., Doan, M.-L., Mitchell, T. M., Toussaint, R., Reuschlé, T., Fondriest, M., Gratier, J.-P., and Renard, F.: Dynamic fracturing by successive coseismic loadings leads to pulverization in active fault zones, J. Geophys. Res.-Sol. Ea., 121, 2338–2360, https://doi.org/10.1002/2015JB012542, 2016.

Aben, F. M., Doan, M. L., Gratier, J.-P., and Renard, F.: Coseismic damage generation and pulverization in fault zones: Insights from dynamic Split-Hopkinson pressure bar experiments, in: Fault zone dynamic processes: evolution of fault properties during seismic rupture, edited by: Thomas, M. Y., Mitchell, T. M., and Bhat, H. S., Geophysical Monograph, 227, American Geophysical Union, John Wiley & Sons, Inc., 2017.

Amitrano, D. and Schmittbuhl, J.: Fracture roughness and gouge distribution of a granite shear band, J. Geophys. Res.-Sol. Ea., 107, 2375, https://doi.org/10.1029/2002JB001761, 2002.

Austrheim, H., Dunkel, K., Plümper, O., Ildefonse, B., Liu, Y., and Jamtveit, B.: Fragmentation of wall rock garnets during deep crustal earthquakes, Sci. Adv., 3, e1602067, https://doi.org/10.1126/sciadv.1602067, 2017.

Bachmann, F., Hielscher, R., and Schaeben, H.: Texture analysis with MTEX–free and open source software toolbox, Solid State Phenom. 160, 63–68, https://doi.org/10.4028/www.scientific.net/SSP.160.63, 2010.

Ben-Zion, Y. and Shi, Z.: Dynamic rupture on a material interface with spontaneous generation of plastic strain in the bulk, Earth Planet. Sc. Lett., 236, 486–496, https://doi.org/10.1016/j.epsl.2005.03.025, 2005.

Blenkinsop, T. G. and Sibson, R. H.: Aseismic fracturing and cataclasis involving reaction softening within core marerial from the Cajon Pass drill hole, J. Geophys. Res., 97, 5135–5144, 1992.

Bouchon, M.: The state of stress on some faults of the San Andreas system as inferred from near-field strong motion data, J. Geophys. Res., 102, 11731–11744, 1997.

Bouchon, M. and Karabulut, H.: The aftershock signature of supershear earthquakes, Science, 320, 1323–1325, https://doi.org/10.1126/science.1155030, 2008.

Bouchon, M. and Vallée, M.: Observation of long supershear rupture during the magnitude 8.1 Kunlunshan earthquake, Science, 301, 824–826, https://doi.org/10.1126/science.1086832, 2003.

Bouchon, M., Bouin, M. P., Karabulut, H., Toksoz, M. N., Dietrich, M., and Rosakis, A. J.: How fast is rupture during an earthquake? New insights from the 1999 Turkey earthquakes, Geophys. Res. Lett., 28, 2723–2726, 2001.

Boullier, A.-M.: Fault zone geology: lessons from drillings through Nojima and Chelungpu faults, in: Geology of the Earthquake Source: A Volume in Honour of Rick Sibson, edited by: Fagereng, A., and Toy, V., Geol. Soc. Spec. Publ., London, UK, 359, 17–37, 2011.

Boullier, A.-M., Ohtani, T., Fujimoto, K., Ito, H., and Dubois, M.: Fluid inclusions in pseudotachylytes from the Nojima fault, Japan, J. Geophys. Res.-Sol. Ea., 106, 21965–21977, 2001.

Boullier, A.-M., Fujimoto, K., Ito, H., Ohtani, T., Keulen, N., Fabbri, O., Amitrano, D., Dubois, M., and Pezard, P.: Structural evolution of the Nojima fault (Awaji Island, Japan) revisited from the GSJ drill hole at Hirabayashi, Earth Planets Space, 56, 1233–1240, 2004a.

Boullier, A.-M., Fujimoto, K., Ohtani, T., Roman-Ross, G., Lewin, E., Ito, H., Pezard, P., and Ildefonse, B.: Textural evidence for recent co-seismic circulation of fluids in the Nojima fault zone, Awaji island, Japan, Tectonophysics, 378, 165–181, 2004b.

Brantley, S. L.: The effect of fluid chemistry on quartz microcrack lifetimes, Earth Planet. Sc. Lett., 113, 145–156, 1992.

Brenguier, F., Campillo, M., Hadziioannou, C., Shapiro, N. M., Nadeau, R. M., and Larose, E.: Postseismic relaxation along the San Andreas fault at Parkfield from continuous seismological observations, Science, 321, 1478–1481, https://doi.org/10.1126/science.1160943, 2008.

Chen, K., Dejoie, C., and Wenk, H.-R.: Unambiguous indexing of trigonal crystals from white-beam Laue diffraction patterns: application to Dauphiné twinning and lattice stress mapping in deformed quartz, J. Appl. Crystallogr., 45, 982–989, https://doi.org/10.1107/S0021889812031287, 2012.

Chen, K., Kunz, M., Tamura, N., and Wenk, H.-R.: Residual stress preserved in quartz from the San Andreas Fault Observatory at Depth, Geology, 43, 219–222, 2015.

Chester, F. M. and Chester, J. S.: Ultracataclasite structure and friction processes of the Punchbowl fault, San Andreas system, California, Tectonophysics, 295, 199–221, 1998.

Cho, M., Maruyama, S., and Liou, J. G.: An experimental investigation of heulandite-laumontite equilibrium at 1000 to 2000 bar Pfluid, Contrib. Mineral. Petr., 97, 40–50, 1987.

Cummings, D.: Kink-bands: shock deformation of biotite resulting from a nuclear explosion, Science, 148, 950–952, 1965.

Dejoie, C., Kunz, M., Tamura, N., Bousige, C., Chen, K., Teat, S., Beavers, C., and Baerlocher, C.: Determining the energy-dependent X-ray flux variation of a synchrotron beamline using Laue diffraction patterns, J. Appl. Crystallogr., 44, 177–183, https://doi.org/10.1107/S0021889810052015, 2011.

Derez, T., Pennock, G., Drury, M., and Sintubin, M.: Low-temperature intracrystalline deformation microstructures in quartz, J. Struct. Geol., 71, 3–23, https://doi.org/10.1016/j.jsg.2014.07.015, 2015.

Diamond, L. W. and Tarantola, A.: Interpretation of fluid inclusions in quartz deformed by weak ductile shearing: reconstruction of differential stress magnitudes and pre-deformation fluid properties, Earth Planet. Sc. Lett., 417, 107–119, 2015.

Dieter, G. E.: Mechanical metallurgy, Material Science and Engineering Series, 2nd Edn., McGraw-Hill, Inc., New York, USA, 774 pp., 1976.

Doan, M. L. and Gary, G.: Rock pulverization at high strain rate near the San Andreas fault, Nat. Geosci., 2, 709–712, 2009.

Dor, O., Ben-Zion, Y., Rockwell, T. K., and Brune, J.: Pulverized rocks in the Mojave section of the San Andreas Fault Zone, Earth Planet. Sc. Lett., 245, 642–654, 2006.

Dor, O., Chester, J. S., Ben-Zion, Y., Brune, J. N., and Rockwell, T. K.: Characterization of damage in sandstones along the Mojave Section of the San Andreas Fault: implications for the shallow extent of damage generation, Pure Appl. Geophys., 166, 1747–1773, 2009.

Fabbri, O., Iwamura, K., Matsunaga, S., Coromina, G., and Kanaori, Y.: Distributed strike-slip faulting, block rotation, and possible intracrustal vertical decoupling in the convergent zone of southwest Japan, in: Vertical Coupling and Decoupling of the Lithosphere, edited by: Grocott, J., Tikoff, B., McCaffrey, K. J. W., and Taylor, G., Geol. Soc. Spec. Publ., London, UK, 227, 141–166, 2004.

Famin, V., Raimbourg, H., Garcia, S., Bellahsen, N., Hamada, Y., Boullier, A.-M., Michon, L., Revil, A., Uchide, T., Ricci, T., Hirono, T., and Kawabata, K.: Stress rotations and the long-term weakness of the Median Tectonic Line and the Rokko-Awaji segment, Tectonics, 33, 1900–1919, https://doi.org/10.1002/2014TC003600, 2014.

Fauré, J.: Recherches sur les effets géologiques d'explosions atomiques souterraines dans un massif de granite saharien, Thèse Doctorat Sciences Naturelles, Faculté des Sciences, Université de Nancy, Nancy, France, 433 pp., 1970.

Fujimoto, K., Ueda, A., Ohtani, T., Takahashi, M., Ito, H., Tanaka, H., and Boullier, A. M.: Borehole water and hydrologic Nojima fault, SW model around the Japan, Tectonophysics, 443, 174–182, 2007.

Grosse-Kunstleve, R. W., Sauter, N. K., Moriarty, N. W., and Adams, P. D.: The Computational Crystallography Toolbox: crystallographic algorithms in a reusable software framework, J. Appl. Crystallogr., 35, 126–136, 2002.

Hickman, S. and Zoback, M.: Stress orientations and magnitudes in the SAFOD pilot hole, Geophys. Res. Lett., 31, L15S12, https://doi.org/10.1029/2004GL020043, 2004.

Hielscher, R. and Schaeben, H.: A novel pole figure inversion method: specification of the MTEX algorithm, J. Appl. Crystallogr., 41, 1024–1037, https://doi.org/10.1107/S0021889808030112, 2008.

Hilgers, C., Köhn, D., Bons, P. D., and Urai, J. L.: Development of crystal morphology during unitaxial growth in a progressive widening vein: II. Numerical simulations of the evolution of antitaxial fibrous veins, J. Struct. Geol., 23, 873–885, 2001.

Hirth, G. and Tullis, J.: The brittle-plastic transition in experimentally deformed quartz aggregates, J. Geophys. Res., 99, 11731–11747, 1994.

Ikeda, R., Iio, Y., and Omura, K.: In situ stress measurements in NIED boreholes in and around the fault zone near the 1995 Hyogo-ken Nanbu earthquake, Japan, Isl. Arc, 10, 252–260, 2001.

Ito, H., Kuwahara, Y., Kiguchi, T., Fujimoto, K., and Ohtani, T.: Outline of the Nojima Fault drilling by GSJ: structure, physical properties and permeability structure from borehole measurements in GSJ borehole crossing the Nojima Fault, Japan, Proceedings of the International workshop on the Nojima fault core and borehole analysis, 22–23 November 1999, Tsukuba, Japan, 71–79, 2000.

Kanaori, Y.: Late Mesozoic-Cenozoic strike-slip and block rotation in the inner belt of Southwest Japan, Tectonophysics, 177, 381–399, 1990.

Kunz, M., Chen, K., Tamura, N., and Wenk, H.-R.: Evidence for residual elastic strain in deformed natural quartz, Am. Mineral., 94, 1059–1062, 2009.

Lin, W., Kwasniewski, M., Imamura, T., and Matsuki, K.: Determination of three-dimensional in situ stresses from anelastic strain recovery measurements of cores at great depth, Tectonophysics, 426, 221–238, 2006.

Lloyd, G. E.: Grain boundary contact effects during faulting of quartzite: an SEM/EBSD analysis, J. Struct. Geol., 22, 1675–1693, 2000.

Lloyd, G. E.: Microstructural evolution in a mylonitic quartz simple shear zone: the significant roles of Dauphiné twinning and misorientation, in: Flow processes in faults and shear zones, edited by: Alsop, G. I., Holdsworth, R. E., McCaffrey, K. J. W., and Hand, M., Geol. Soc. Spec. Publ., London, UK, 224, 39–61, 2004.

Lockner, D. A., Tanaka, H., Ito, H., Ikeda, R., Omura, K., and Naka, H.: Geometry of the Nojima Fault at Nojima-Hirabayashi, Japan – I. A Simple Damage Structure Inferred from Borehole Core Permeability, Pure Appl. Geophys., 166, 1649–1667, 2009.

Mainprice, D., Lloyd, G. E., and Casey, M.: Individual orientation measurements in quartz polycrystals – Advantages and limitations for texture and petrophysical property determinations, J. Struct. Geol., 15, 1169–1187, 1993.

Mainprice, D., Bachmann, F., Hielscher, R., and Schaeben, H.: Descriptive tools for the analysis of texture projects with large datasets using MTEX: strength, symmetry and components, in: Rock Deformation from Field, Experiments and Theory: A Volume in Honour of Ernie Rutter, edited by: Faulkner, D. R., Mariani, E., and Mecklenburgh, J., Geol. Soc. Spec. Publ., London, UK, 409, 251–271, 2014.

Menegon, L., Piazolo, S., and Pennacchioni, G.: The effect of Dauphiné twinning on plastic strain in quartz, Contrib. Mineral. Petr, 161, 635–652, 2011.

Mitchell, T. M., Ben-Zion, Y., and Shimamoto, T.: Pulverized fault rocks and damage asymmetry along the Arima-Takatsuki Tectonic Line, Japan, Earth Planet. Sc. Lett., 308, 284–297, https://doi.org/10.1016/j.epsl.2011.04.023, 2011.

Murakami, M. and Tagami, T.: Dating pseudotachylyte of the Nojima fault using the zircon fission-track method, Geophys. Res. Lett., 31, L12604, https://doi.org/10.1029/2004GL020211, 2004.

Nédélec, A. and Bouchez, J.-L.: Pétrologie des granites: structure, cadre géologique, Interactions, edited by: De Wever, P., Société Géologique de France, Vuibert, Paris, France, 306 pp., 2011.

Nicolas, A. and Poirier, J.-P.: Crystalline plasticity and solid-state flow in metamorphic rocks, J. Wiley Interscience Publications, London, UK, 444 pp., 1976.

Ogi, H., Ohmori, T., Nakamura, N., and Hirao, M.: Elastic, anelastic, and piezoelectric coefficients of α-quartz determined by resonnance ultrasound spectroscopy, J. Appl. Phys., 100, 053511, https://doi.org/10.1063/1.2335684, 2006.

Ohtani, T., Fujimoto, K., Ito, H., Tanaka, H., Tomida, N., and Higuchi, T.: Fault rocks and past to recent fluid characteristics from the borehole survey of the Nojima fault ruptured in the 1995 Kobe earthquake, southwest Japan, J. Geophys. Res., 105, 16161–16171, 2000a.

Ohtani, T., Miyazaki, T., Tanaka, H., Kiguchi, T., Fujimoto, K., and Ito, H.: Reorientation of cores and distribution of macroscopic fractures along the GSJ borehole penetrating the Nojima fault zone, International workshop of the Nojima fault core and borehole data analysis, Tsukuba, Japan, 22–23 November 1999, 271–276, 2000b.

Pêcher, A.: Experimental decrepitation and reequilibration of fluid inclusions in synthetic quartz, Tectonophysics 78, 567–584, 1981.

Pehl, J. and Wenk, H.-R.: Evidence for regional Dauphiné twinning in quartz from the Santa Rosa mylonite zone in Southern California. A neutron diffraction study, J. Struct. Geol., 27, 1741–1749, 2005.

Petit, J., Castelnau, O., Bornert, M., Zhang, F. G., Hofmann, F., Korsunsky, A. M., Faurie, D., Le Bourlot, C., Micha, J. S., Robach, O., and Ulrich, O.: Laue-DIC: a new method for improved stress field measurements at the micrometer scale, J. Synchrotron Radiat., 22, 980–994, https://doi.org/10.1107/S1600577515005780, 2015.

Reches, Z. and Dewers, T. A.: Gouge formation by dynamic pulverization during earthquake rupture, Earth Planet. Sc. Lett., 235, 361–374, https://doi.org/10.1016/j.epsl.2005.04.009, 2005.

Robach, O., Micha, J.-S., Ulrich, O., Devincre, B., Hoc, T., Daveau, G., Consonni, V., and Petit, J.: Analyse avancée des des contraintes et des gradients d'orientation par microdiffraction Laue des rayons X, in: Rayons X et Matière 5, RX2013, edited by: Guinebretière, R., and Goudeau, P., ISTE Editions, London, UK, 83–147, 2017.

Rockwell, T., Sisk, M., Girty, G., Dor, O., Wechsler, N., and Ben-Zion, Y.: Chemical and Physical Characteristics of Pulverized Tejon Lookout Granite Adjacent to the San Andreas and Garlock Faults: Implications for Earthquake Physics, Pure Appl. Geophys., 166, 1725–1746, 2009.

Roedder, E.: Fluid inclusions, Reviews in Mineralogy, 12, Mineral. Soc. Am., USA, 644 pp., 1984.

Rosakis, A. J., Xia, K., Lykotrafitis, G., and Kanalori, H.: Dynamic shear rupture in frictional interfaces: speeds, directionality, and modes, in: Treatise of Geophysics, Elsevier, 153–192, 2007.

Sagy, A. and Korngreen, D.: Dynamic branched fractures in pulverized rocks from a deep borehole, Geology, 40, 799–802, 2012.

Savage, J. C. and Wood, M. D.: The relation between apparent stress and stress drop, B. Seismol. Soc. Am., 61, 1381–1388, 1971.

Shamir, G. and Zoback, M. D.: Stress orientation profile to 3.5 km depth near the San Andreas Fault at Cajon Pass, California, J. Geophys. Res., 97, 5059–5080, 1992.

Sherby, O. D., Klundt, H. R., and Miller, A. K.: Flow stress, subgrain size, and subgrain stability at elevated temperature, Metall. Trans. A, 8, 843–850, 1977.

Shi, Z. and Ben-Zion, Y.: Dynamic rupture on a bimaterial interface governed by slip-weakening friction, Geophys. J. Int., 165, 469–484, https://doi.org/10.1111/j.1365-246X.2006.02853.x, 2006.

Sibson, R. H.: Fault rocks and fault mechanisms, J. Geol. Soc. London, 133, 191–213, 1977.

Sibson, R. H.: Thickness of the seismic slip zone, B. Seismol. Soc. Am., 93, 1169–1178, 2003.

Stünitz, H., Thust, A., Heilbronner, R., Behrens, H., Kilian, R., Tarantola, A., and Fitz Gerald, J. D.: Water redistribution in experimentally deformed natural milky quartz single crystals – Implications for H2O-weakening processes, J. Geophys. Res.-Sol. Ea., 122, 866–894, https://doi.org/10.1002/2016JB013533, 2017.

Sullivan, W. A. and Peterman, E. M.: Pulverized granite at the brittle-ductile transition: an exemple from the Kellyland fault zone, eastern Maine, USA, J. Struct. Geol., 101, 109–123, https://doi.org/10.1016/j.jsg.2017.07.002, 2017.

Tamura, N.: XMAS: a versatile tool for analyzing synchrotron X-ray microdiffraction data, in: Strain and dislocation gradients from diffraction, edited by: Barabash, R. I., and Ice, G. E., Imperial College Press/World Scientific Publishing, 125–155, 2014.

Tanaka, H., Fujimoto, K., Ohtani, T., and Ito, H.: Structural and chemical characterization of shear zones in the freshly activated Nojima fault, Awaji Island, southwest Japan, J. Geophys. Res., 106, 8789–8810, 2001.

Tarantola, A., Diamond, L. W., and Stunitz, H.: Modification of fluid inclusions in quartz by deviatoric stress I: experimentally induced changes in inclusion shapes and microstructures, Contrib. Mineral. Petr., 160, 825–843, 2010.

Trepmann, C. A.: Shock effects and pre-shock microstructures in hydrothermal quartz veins from the Rochechouart impact structure, France, J. Struct. Geol., 31, 1183–1196, https://doi.org/10.1016/j.jsg.2009.06.017, 2009.

Trepmann, C. A. and Stöckert, B.: Cataclastic deformation of garnet: a record of synseismic loading and postseismic creep, J. Struct. Geol., 24, 1845–1856, 2002.

Trepmann, C. A. and Stöckhert, B.: Short-wavelength undulatory extinction in quartz recording coseismic deformation in the middle crust – an experimental study, Solid Earth, 4, 263–276, https://doi.org/10.5194/se-4-263-2013, 2013.

Trepmann, C. A., Hsu, C., Hentschel, F., Döhler, K., Schneider, C., and Wichmann, V.: Recrystallization of quartz after low-temperature plasticity – The record of stress relax-

ation below the seismogenic zone, J. Struct. Geol., 95, 72–92, https://doi.org/10.1016/j.jsg.2016.12.004, 2017.

Tullis, J.: Deformation of granitic rocks: experimental studies and natural examples, in: Plastic deformation of minerals and rocks, edited by: Karato, S.-I., and Wenk, H.-R., Rev. Mineral. Geochem., 51, Mineral. Soc. Am., Geochem. Soc., USA, 51–95, 2002.

Ulrich, O., Biquard, X., Bleuet, P., Geaymond, O., Gergaud, P., Micha, J. S., Robach, O., and Rieutord, F.: A new white beam X-ray microdiffraction setup on the BM32 beamline at the European Synchrotron Radiation Facility, Rev. Sci. Instrum., 82, 033908, https://doi.org/10.1063/1.3555068, 2011.

Wechsler, N., Allen, E. E., Rockwell, T. K., Girty, G., Chester, J. S., and Ben-Zion, Y.: Characterization of pulverized granitoids in a shallow core along the San Andreas Fault, Littlerock, CA, Geophys. J. Int., 186, 401–417, https://doi.org/10.1111/j.1365-246X.2011.05059.x, 2011.

Wenk, H.-R., Lonardelli, I., Vogel, S. C., and Tullis, J.: Dauphiné twinning as evidence for an impact origin of preferred orientation in quartzite; an example from Vredefort, South Africa, Geology, 33, 273–276, 2005.

Wenk, H.-R., Rybacki, E., Dresen, G., Lonardelli, I., Barton, N., Franz, H., and Gonzalez, G.: Dauphiné twinning and texture memory in polycrystalline quartz. Part 1: Experimental deformation of novaculite, Phys. Chem. Miner., 33, 667–676, 2006.

Wenk, H.-R., Janssen, C., Kenkmann, T., and Dresen, G.: Mechanical twinning in quartz: shock experiments, impact, pseudotachylites and fault breccias, Tectonophysics, 510, 69–79, 2011.

Xia, K., Nasseri, M. H. B., Mohanty, B., Lu, F., Chen, R., and Luo, S. N.: Effects of microstructures on dynamic compression of Barre granite, Int. J. Rock Mech. Min., 45, 879–887, 2008.

Yuan, F., Prakash, V., and Tullis, T.: Origin of pulverized rocks during earthquake fault rupture, J. Geophys. Res.-Sol. Ea., 16, B06309, https://doi.org/10.1029/2010JB007721, 2011.

Zamora, M., Pézard, P. A., and Ito, H.: Anisotropy of elastic and anelastic properties of granites from the Hirabayashi hole, Japan, International workshop of the Nojima fault core and borehole data analysis, 22–23 November 1999, Tsukuba, Japan, 227–231, 2000.

Zhang, Q. B. and Zhao, J.: A review of dynamic experimental techniques and mechanical behaviour of rock materials, Rock Mech. Rock Eng., 47, 1411–1478, https://doi.org/10.1007/s00603-013-0463-y, 2014.

Zoback, M. D. and Healy, J. H.: In situ measurements to 3.5 km depth in the Cajon Pass scientific research borehole: implications for the mechanics of crustal faulting, J. Geophys. Res., 97, 5039–5057, 1992.